Probabilistic Analysis of Meanline Compressor Rotor Performance

by

Nathan Andrew Fitzgerald

B.S., Massachusetts Institute of Technology (2002)

Submitted to the Department of Aeronautics and Astronautics
in partial fulfillment of the requirements for the degree of

Master of Science in Aeronautics and Astronautics

at the

MASSACHUSETTS INSTITUTE OF TECHNOLOGY

August 2004
[September 2004]

© Massachusetts Institute of Technology 2004. All rights reserved.

Author ....
Department of Aeronautics and Astronautics
August 6, 2004

Certified by........ ......
Edward M. Greitzer
H. N. Slater Professor of Aeronautics and Astronautics
Thesis Supervisor

Accepted by ....
Jaime Peraire
Professor of Aeronautics and Astronautics
Chair, Committee on Graduate Students

MASSACHUSETTS INSTITUTE
OF TECHNOLOGY
FEB 10 2005
LIBRARIES

AERO

Probabilistic Analysis of Meanline Compressor Rotor Performance

by

Nathan Andrew Fitzgerald

Submitted to the Department of Aeronautics and Astronautics
on August 6, 2004, in partial fulfillment of the
requirements for the degree of
Master of Science in Aeronautics and Astronautics

Abstract

This thesis addresses variability in aerodynamic performance of a compressor rotor due to geometric variation. The performance of the rotor is computed using a meanline model that includes the effect of tip clearance blockage, calculated by assuming the tip leakage behaves like a wake in a pressure gradient and incorporating the effects of double leakage. The model is used to quantify performance variability of the rotor at design flow coefficient and near stall given typical variations in blade profile geometry, hub and casing diameters, and tip clearances. Monte Carlo simulation performed at both operating conditions shows that the coefficient of variation of pressure rise, loss coefficient, axial displacement thickness, and flow angle at the exit of the blade row is similar at high and low loading. Mean shifts are smaller at design than near stall, where the mean pressure rise and loss shift -0.4% and +0.6% from their respective nominal values. A parametric analysis using a response surface showed that near stall, tip clearance variation drives performance variation; the pressure rise and loss coefficient standard deviation drop by 26% and 20% when tip clearance variability is removed. At design, tip clearance variability is still important, but leading and trailing edge blade geometries play a larger role in driving performance variability.

Thesis Supervisor: Edward M. Greitzer
Title: H. N. Slater Professor of Aeronautics and Astronautics

Acknowledgments

I must extremely grateful to Prof. Edward Greitzer for his patience and guidance while serving as the advisor to this project. The academic and financial support I enjoyed as a result of his efforts during my stay at MIT have been immensely appreciated. The recommendations and suggestions of Professors David Darmofal, Dan Frey, Ian Waitz, and Karen Wilcox during Robust Jet Engines meetings was also greatly appreciated. Thanks to Mark Drela and Ali Merchant for answering question about aerodynamics and helping me understand and implement MISES. Special thanks goes to to Victor Garzon for always being available, willing, and eager to help me work out with any issue I presented to him.

I am also grateful for the support of the students, faculty, and staff of the Gas Turbine Lab and Aero–Astro department. Thanks go to my officemates Boris Sirakov, Juan Castiella, and Vei–man Lei for offering their suggestions and assistance on almost every issue I faced, be it mundane or complicated. Thanks also go to the "lunch crew," Garrett Barter, Todd Oliver, Mike Brasher, Alex Mozdzanowska, Mark Monroe, and Shana Diez for putting that extra bit of fun into my graduate school experience. Special thanks go to mother and brother, who have always had so much faith in me even when I doubted myself, and to Sabrin Mohamed, whose support these last two years has been invaluable.

Support for this work was provided by the SNECMA Moteurs and MIT Collaborative (Agreement No. 12/01/01/-924205781), NASA Glenn Research Center though grant No. NAG3-2320, the H. N. Slater Professorship, and a Department of Aeronautics and Astronautics Fellowship. All sources are gratefully acknowledged.

Contents

1 Introduction **19**

1.1 Background & Motivation 19

1.2 Previous Studies 20

1.2.1 Compressor Performance Variability 20

1.2.2 Blockage Definition and Modeling 20

1.3 Thesis Objectives 22

1.4 Approach 22

1.5 Contributions 23

1.6 Thesis Outline 23

2 Meanline Flow Model with Tip Clearance Effects **25**

2.1 Overview 25

2.2 Core Flow Module 27

2.3 Endwall Flow Module 28

2.3.1 Estimation of AVDR 29

2.3.2 Endwall Loss 31

2.4 Flow Feature Overview 32

2.4.1 Leakage Jet 32

2.4.2 Jet-Freestream Interaction 33

2.4.3 Double Leakage and Clearance Gap P_t 34

2.5 Tip Clearance Blockage Calculation 36

2.5.1 Calculation Overview 36

2.5.2 New Developments in the Tip Clearance Model 38

2.6 Flow Feature Refinement 39

2.6.1 Total Pressure Correlation 39
2.6.2 Leakage Angle Refinement 41
2.7 Inlet Defect Evolution Calculation 42
2.8 Assessment of Model Performance 46
2.9 Chapter Summary 48

3 Analytical Framework and Probabilistic Approach 49
3.1 Rotor Geometry 49
3.1.1 Nominal Performance 51
3.2 Variability Quantification 52
3.2.1 Geometric Variability 52
3.2.2 Performance Variability 53
3.3 Monte Carlo Simulation 54
3.3.1 Repeated Latin Hypercube Sampling 55
3.3.2 Response Surface Modeling 56
3.4 Chapter Summary 57

4 Analysis Results 59
4.1 Variability Characterization 59
4.2 Assessment of the Key Drivers of Variability 63
4.2.1 RSM Fit Assessment 63
4.2.2 Parametric Analysis 67
4.3 Sensitivity Comparison 69
4.4 Comparison with Previous Work 70
4.5 Summary 71

5 Conclusion 73
5.1 Thesis Summary 73
5.2 Recommendations for Future Work 74

A Integral Wake Calculation 75
A.1 Inviscid Representation 76
A.2 Viscous Representation 78
A.3 Quasi-Simultaneous Coupling 79

B RSM and Meanline Model CDF Comparison **81**

Bibliography **85**

List of Figures

1-1 Diagram of blockage region 22

2-1 Meanline Model Diagram 26
2-2 Leakage Angle Calculation 33
2-3 Streamlines released from clearance gap 34
2-4 Interaction line control volume 35
2-5 Reduction in $C_{p_t} = \frac{P_t - P_{t_1}}{P_{t_1} - P_1}$ due to double leakage 36
2-6 Blockage model diagram 37
2-7 Clearance gap total pressure profiles 40
2-8 Leakage angle model comparison 42
2-9 Pressure side leakage flow angle correlation 43
2-10 Diffuser Analogy 44
2-11 Defect skew due to shift of reference frames 45
2-12 Blockage model comparison with data from Lavainne[27] 47

3-1 Rotor geometry dimensions 50
3-2 Rotor total-to-static characteristic 52
3-3 Illustration of probabilistic performance metrics 54
3-4 Latin hypercube sample construction 56

4-1 On–design performance variability 61
4-2 Near–stall performance variability 62
4-3 Response surface method (RSM) vs. model for design conditions 65
4-4 Response surface method (RSM) vs. model for near-stall conditions 66
4-5 C_p variability drivers 67
4-6 ω variability drivers 68

4-7 δ_z^* variability drivers 68
4-8 α_2 variability drivers 69
4-9 ψ_{stall} variability drivers 69

A-1 Viscous and inviscid wake representations used in Veldman[39] quasi-simultaneous coupling method 77

B-1 Response surface method (RSM) vs model CDF at near-stall condition . . . 81
B-2 Response surface method (RSM) vs model CDF at design condition 82

List of Tables

3.1 Geometry Specification 50

3.2 Design Velocity Triangle Specifications 50

3.3 Rotor nominal performance 51

3.4 Rotor Geometric variability 53

4.1 On–design performance variability 60

4.2 Near–stall performance variability 60

4.3 RSM on–design performance variability 64

4.4 RSM near–stall performance variability 64

4.5 Performance Sensitivity, $\frac{\partial(performance)}{\partial(geometry)}$ 70

Nomenclature

A	Area
A_b	Blockage
C_d	Dissipation coefficient, $\frac{1}{\rho v_e^3} \int \tau \frac{\partial v}{\partial y} dy$
C_p	Static pressure coefficient, $(P - P_1)/(P_{t_1} - P_1)$
C_{p_t}	Total pressure coefficient, $(P_t - P_{t_1})/(P_{t_1} - P_1)$
H	Shape factor, δ^*/θ
H^*	Kinetic energy shape factor, θ^*/θ
I	Rothalpy
K_p	Turbulent eddy viscosity coefficient
P	Pressure
$Q_{5\%}, Q_{95\%}$	5% and 95% quantiles
R	Radius
T	Temperature
U	Wheel speed at meanline
b	Blade span
c	Chord
g	Solidity

$\dot{m}$	Massflow
r, θ, z	Cylindrical coordinates. Radial, tangential, and axial directions
t_{max}	Maximum blade thickness
v	Velocity
x_{dbl}	The distance from the leading edge where the jet-freestream interaction line from one blade impinges on the next blade in the row.
α	Leakage jet flow angle, measured from the chord line. Swirl angle in the stationary frame, measured from the axial direction.
β	Blade relative swirl angle or blade camber line angle, measured from the axial direction.
δ	Boundary layer thickness
δ^*	Displacement thickness
θ	Displacement thickness. Angle between jet-freestream interaction line and chord.
θ^*	Kinetic energy thickness
μ	Statistical mean
ρ	Density
σ	Standard deviation
τ	Tip clearance gap height
ϕ	Flow coefficient, v_z/U
Ω	Angular velocity

Subscripts

$()_{cs}, ()_{hub}$	Condition at casing and hub
$()_{le}, ()_{te}$	Condition at leading edge and trailing edge

$()_{mean}$	Condition at meanline radius
$()_{ss}, ()_{ps}$	Condition at suction and pressure sides of the blade.
$()_{sw}$	Streamwise direction
$()_t$	Stagnation quantity
$()_1, ()_2$	Condition upstream and downstream of the blade row

Acronyms

AVDR	Axial Velocity Density Ratio
CDF	Cumulative Density Function
DCA	Double Circular Arc
MCS	Monte Carlo Simulation
MISES	Multiple blade Interactive Streamtube Euler Solver
ODE	Ordinary Differential Equation
PDF	Probability Density Function
RANS	Reynolds Averaged Navier-Stokes
RSM	Response Surface Model

Chapter 1

Introduction

1.1 Background & Motivation

In the past few decades, gas turbine engine technology has matured to the point where gains have begun to asymptote for traditional component performance metrics[17]. Many opportunities exist, however, for improvements in performance metrics such as reliability, maintainability, and operability to make a profound impact on future gas turbine engine evolution.

One such metric is robustness, defined here as a measure of the variability in system performance from the design intent due to factors such as manufacturing variation, deterioration, and operational variation. A robust system has a small output variability for a given input variability, and, as defined in this thesis, the goal of robust design is to limit the effect of variation in system inputs on the overall performance. Rather than restricting the variability of the inputs to reduce the output variability (for example, by reducing manufacturing tolerances), design changes are sought that reduce performance sensitivity to the same input variation.

Robust design practices became popular in the 1980's with the advent of the Taguchi method[6], used primarily in manufacturing quality control. In the gas turbine industry, probabilistic methods have traditionally been used in structural design, particularly concerning high cycle fatigue[29]. Only recently have robust practices been applied to aerothermal design[15, 32].

An obstacle to robust aerodynamic design is the computational requirements of probabilistic analyses, which typically require thousands of simulations of a system. The large computational cost of a single high fidelity 3D RANS simulation makes it an unreasonable tool for robust design at current processor speeds. In order for a probabilistic analysis to be tractable, therefore, reduced order models that capture the performance trends must be employed.

This thesis focuses on the characterization of variability in aerodynamic performance of a compressor rotor as part of an effort to i) define the key drivers of variability and ii) develop a robust design philosophy. A reduced order computational model, including endwall effects, is used to simulate the performance of a single rotor for a given nominal geometry. A probabilistic analysis is then performed where the geometry is allowed to vary from the nominal depending on manufacturing tolerances. The variation in performance and the role of the individual geometric parameters is then assessed.

1.2 Previous Studies

1.2.1 Compressor Performance Variability

Garzon and Darmofal[15] quantified the variability in the profile shape of an integrally-bladed rotor by conducting a statistical analysis of a set of high resolution blade surface measurements. Probabilistic analysis using Monte Carlo simulation was performed using a meanline model of the rotor. The analysis was entirely two-dimensional, with no endwall effects included. For the conditions tested, up to 20% mean shifts in turning and loss were reported.

Lavainne[27] conducted deterministic and probabilistic performance analyses of an embedded compressor stage, subject to blade geometric variations. Performance sensitivities were calculated using 3D RANS computations as well as a meanline model that included correlations for endwall effects. Tip clearances were found to be the most important drivers of variation in the 3D computations, but were less important in the meanline model. The difference between the models was attributed to the inability of the meanline analysis to capture the different trends in endwall flow blockage exhibited by the rotor and stator.

1.2.2 Blockage Definition and Modeling

Endwall blockage and loss have long been understood to be important factors in compressor performance, particularly with regards to maximum pressure rise[5]. Blockage is the reduction in effective flow area due to velocity defects in a compressor. It is the 3D version of the concept of a displacement thickness for a boundary layer. Unlike a two-dimensional boundary layer, however, the flow field of a axial compressor offers no simple choices for defect region and reference freestream velocity for which to base a blockage calculation. Therefore, the definition and use of the term has been interpreted differently by different researchers.

For an axisymmetric or pitch averaged view of compressor flow, blockage can be defined in terms of axial displacement thickness,

$$\delta_z^* = \int_0^\delta 1 - \frac{\rho v}{\rho_e v_e} dr, \tag{1.1}$$

a direct analogy with a boundary layer. The definitions of boundary layer thickness, δ, and the edge density and velocity, ρ_e and v_e, however, vary among various authors[20, 21, 33, 35].

Smith[35] and Koch and Smith[26] presented axial displacement thickness correlations based on a repeating stage analysis. Tip clearance gap height, staggered spacing, pressure rise, and stalling pressure rise are inputs. This correlation was used by Lavainne, who estimated the stalling pressure rise using the correlation of Koch[25].

Khalid[22] proposed the following definition for blockage:

$$A_b = \int_A 1 - \frac{\rho v_{sw}}{\rho_e v_e} dA. \tag{1.2}$$

The integration is performed over the blocked region, A, diagrammed in Figure 1-1, whose boundaries are determined from the magnitude of the gradient, $|\nabla(\rho v_{sw})|$. Constant value contours of the gradient are calculated on the exit plane of a given blade row, and an arbitrary cut–off value is chosen to define the blocked region. The edge velocity and density, v_e and ρ_e, are the values on the defect boundary closest to dA.

Using this definition, Khalsa[23] conducted a parametric study of tip clearance blockage trends due to design parameter variations. The behavior of the blockage due to tip clearance flow was modeled as a wake in a pressure gradient. From comparisons with 3D numerical simulations and low speed compressor experiments, Khalsa showed that the model captured trends with tip clearance gap height, loading level, and solidity.

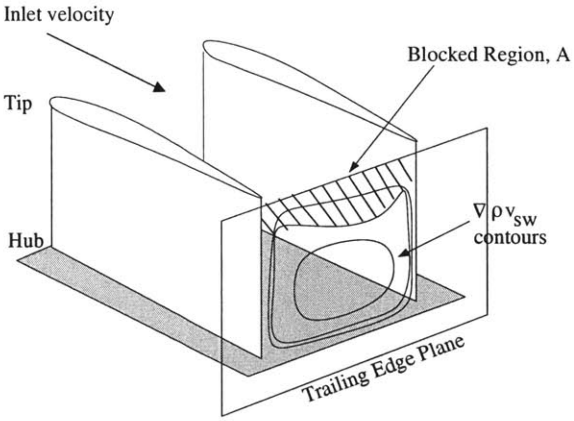

Figure 1-1: Diagram of blockage region

1.3 Thesis Objectives

The goals of this thesis are to:

- Quantify the variability in rotor pressure rise, loss, and stalling pressure rise due to variations in blade row geometry at design and near–stall conditions.
- Identify the key drivers of rotor performance variability at design and near–stall conditions.

1.4 Approach

This thesis builds on the work of Garzon[14] and Lavainne[27]. The major conceptual extension is the incorporation of an endwall model which is tied more closely to the dominant fluid dynamic mechanisms into a meanline analysis. Meanline blade performance is determined from a fast running, quasi-2D cascade analysis program. Whereas Lavainne used a simplified description by Horlock[19] to determine the change in axial displacement thickness across the rotor, the approach to tip clearance blockage taken here is to apply a wake-in-a-pressure-gradient model. Blockage related to tip clearance effects near the casing only is included; hub boundary layers and corner stall are neglected.

The meanline model is used to conduct a probabilistic analysis of a low speed rotor. The geometry of the rotor is varied in a Monte Carlo simulation (MCS), producing a probabilistic performance distribution. The simulation time is smaller than a full RANS calculation, but still large enough to make parametric studies of rotor variability unwieldy. Therefore, the impact of the variability in each geometric parameter is assessed using Monte Carlo simulations run on a response surface representation of the meanline-with-clearance-blockage model.

1.5 Contributions

The primary contributions of this thesis are summarized as follows:

- An existing model for tip clearance blockage was modified to allow blockage estimates to be obtained using the conditions upstream of the blade row as inputs. This included the addition of double leakage effects into the model.
- A meanline rotor performance, including this endwall description, was implemented for use in probabilistic analysis.
- The performance variability of a rotor both at design and near stall conditions was quantified and the key drivers identified.

1.6 Thesis Outline

Chapter 2 presents the meanline model. Chapter 3 defines the probabilistic tools and computational framework. Chapter 4 presents the results of the probabilistic analysis. Chapter 5 presents conclusions and recommendations for future work.

Chapter 2

Meanline Flow Model with Tip Clearance Effects

2.1 Overview

This chapter presents the meanline calculation used to conduct the probabilistic analysis. The flow properties downstream of the blade row are determined given the upstream properties and operating condition. The downstream flow of information in this procedure means the application is for subsonic flow.

A meanline model takes a quasi-1D view of the compressor. Pressure, temperature, Mach number, and flow angle are defined on the "mean radius" and are taken to represent the state of the flow at that axial location in the compressor. Further, the state is only queried at the inlet and exit of the blade row. The details of the flow development are thus condensed into a small set of performance parameters that define the operation of the blade row: loss, flow turning, and axial velocity density ratio (AVDR $= (\rho_2 v_{z_2})/(\rho_1 v_{z_1})$).

The flow turning is determined from the blade geometry by correlation or computation. Losses come from a variety of sources, such as boundary layers on the metal surfaces, tip leakage flows, and corner separation, with magnitudes often taken from correlations. The AVDR is due to the change in the effective cross-sectional area of the passage. Conservation of mass across the row is $(\rho_2 v_{z_2})/(\rho_1 v_{z_1}) = A_{eff_2}/A_{eff_1}$. The effective area of the passage is the area from the hub to the casing minus the blockage caused by nonuniformity in ρv_z. The hub and casing geometry are specified by the design of the machine, but the blockage,

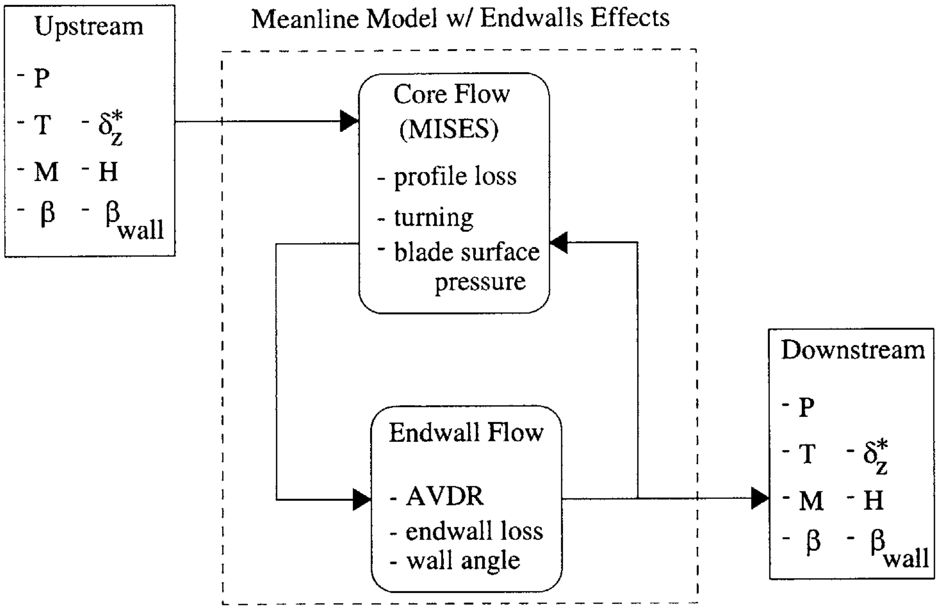
Upstream
- P
- T - δ*z
- M - H
- β - βwall
Meanline Model w/ Endwalls Effects
Core Flow
(MISES)
- profile loss
- turning
- blade surface pressure
Endwall Flow
- AVDR
- endwall loss
- wall angle
Downstream
- P
- T - δ*z
- M - H
- β - βwall

Figure 2-1: Meanline Model Diagram
Determination of static pressure, temperature, Mach number, flow angle (relative to the blade row), axial displacement thickness, endwall flow shape factor, and flow angle at the casing from the meanline model with endwall effects given upstream conditions

which depends on both geometry and operating condition, is typically determined from correlation.

In the present meanline description, the effect of the endwall flow on the AVDR and losses of a blade row are calculated from a model for the endwall flow, rather than a correlation. The pressure, P; temperature, T; Mach number, M; flow angle, β; axial displacement thickness, δ_z^*; shape factor, H; and flow angle at the wall, β_{wall}, define the state of the flow. The process for determining the downstream flow conditions is diagramed in Figure 2-1. The model is broken up into modules for the core and endwall regions. The core refers to flow near the meanline, and the endwall describes the defect flow near the casing.

The core flow parameters depend on the AVDR and the endwall losses, and the endwall model depends on the state parameters set by the core model, so a solution is attained iteratively. Given the blade relative inlet conditions and a guess for the AVDR, the core module determines the meanline blade performance. Given that blade performance, the endwall module then determines the AVDR and the endwall losses, which are used to update the core model's initial guess. The process is iterated until the AVDR converges.

The remainder of this chapter details the core and endwall calculations. Sections 2.2 and 2.3 describe the core and endwall modules respectively. Section 2.4 describes flow features modeled in the tip clearance flow portion of the blockage calculation and Section 2.6 describes required refinements of those flow feature models. Two parts of the endwall module, the tip clearance blockage and inlet defect evolution though the blade row, are described in Sections 2.5 and 2.7. Section 2.8 compares the blockage model with data from computations to assess the validity of the assumptions.

2.2 Core Flow Module

The core module is responsible for determining the downstream pressure, temperature, Mach number, and flow angle on the meanline given the upstream flow and the blade row performance. The meanline performance is defined by flow turning, $\beta_1 - \beta_2$; AVDR, A_{eff_2}/A_{eff_1}; meanline loss coefficient, ω; and total entropy generated in the blade row, s_{gen}/c_p. The meanline loss coefficient, ω, accounts for the total pressure losses at the meanline radius, while s_{gen}/c_p accounts for the losses throughout the passage, which includes meanline loss. The downstream parameters P_2, T_2, and M_2 are determined by the following system of equations:

$$\frac{\dot{m}\sqrt{T_t}}{P_{t_2}A_{eff_2}\cos\beta_2} = \sqrt{\frac{\gamma}{R}}\frac{M_2}{(1+\frac{\gamma-1}{2}M_2^2)^{\frac{\gamma+1}{2(\gamma+1)}}} \tag{2.1}$$

$$c_pT_{t_1} - \frac{1}{2}\Omega^2 r^2_{mean_1} = I_1 = I_2 = c_pT_{t_2} - \frac{1}{2}\Omega^2 r^2_{mean_2} \tag{2.2}$$

$$P_{t_2} = P_{t_1}\left(\frac{T_{t_2}}{T_{t_1}}\right)^{\frac{\gamma}{\gamma-1}} - \omega(P_{t_1} - P_1) \tag{2.3}$$

where

$$A_{eff} = \pi((r_{cs} - \delta_z^*)^2 - r_{hub}^2) \tag{2.4}$$

$$P_t = P\left(1+\frac{\gamma-1}{2}M^2\right)^{\frac{\gamma}{\gamma-1}} \qquad T_t = T\left(1+\frac{\gamma-1}{2}M^2\right).$$

The stagnation quantities in Equations 2.1-2.3 are computed in the rotor frame of reference at the mean radius. Equation 2.1 is the conservation of mass. Equation 2.2 states that rothalpy is conserved. Equation 2.3 is a restatement of the definition of the loss coefficient

$$\omega = \frac{P_{t_{isentropic}} - P_{t_2}}{P_{t_1} - P_1}.$$

The exit flow angle β_2 and the meanline loss coefficient ω are calculated using MISES (Multiple blade Interacting Streamtube Euler Solver), a software package for cascade analysis and design[9]. MISES is capable of analyzing subsonic, transonic, and supersonic flows. Profile losses are determined using an viscous-inviscid integral boundary layer formulation with an e^9 type transition prediction[8]. In the present procedure, MISES is provided with the upstream blade relative Mach number, flow angle, and Reynolds number, along with the blade airfoil geometry on the meanline. The effective streamtube height is input as a function of distance along the meanline, assumed to vary linearly from the inlet to exit of the blade row.

The effective area at the exit of the blade row and the spanwise mixing losses are determined by the iterative coupling with the endwall module in Section 2.3. The endwall module calculates these quantities as functions of the pressure rise, flow turning, and blade surface static pressure along the pressure and suction sides of the blade (which MISES provides).

2.3 Endwall Flow Module

The endwall module determines the AVDR and the endwall losses. The flow near the casing at the exit of a blade row is influenced by two factors. The first is the development of the upstream flow nonuniformity though the passage. The second is the generation of nonuniformity due to tip clearance leakage flow.

The endwall blockage model is broken into two parts to address the two factors that influence the exit endwall flow: i) the evolution of upstream defect through the blade row and ii) the production of tip clearance blockage in the rotor. Each part uses the pressure rise and turning calculated from the core flow module and the geometry of the passage as inputs, and outputs blockage, momentum area, and entropy generated. The tip clearance blockage calculation also takes the static pressure on the blade pressure and suction surfaces as an input. The flow is assumed to be incompressible and the geometry of the passage is simplified to that of a cascade with the same meanline solidity and passage height. The tip clearance flow calculation is described in Section 2.5.1 and the evolution of the upstream defect is described in Section 2.7.

The components of the endwall blockage, momentum area, and entropy from i) and ii) are thus calculated separately, although in a real machine the factors they represent are coupled. The blockage is defined in Equation 1.2, and a related quantity, the momentum area is defined as

$$A_m = \int_A \frac{\rho v_{sw}}{\rho_e v_e} \left(1 - \frac{v_{sw}}{v_e}\right) dA. \tag{2.5}$$

The quantity A_m measures the momentum deficit in the blocked region (analogous to momentum thickness in two dimensions). The results of blockage, momentum area, and entropy from the two parts of the endwall module are summed to determine the values of those quantities at the exit of the passage. The AVDR and endwall loss are then calculated based on a series of assumptions, described in Sections 2.3.1 and 2.3.2.

2.3.1 Estimation of AVDR

The effective passage area used in the core flow module is given by

$$A_{eff} = \pi((r_{cs} - \delta_z^*)^2 - r_{hub}^2) \tag{2.4}$$

The use of Equation 2.4 for the AVDR is based on an axisymmetric description of the annulus flow, although the endwall model does not have this restriction. The axial displacement thickness is defined as

$$\delta_z^* = \frac{1}{R_{cs}} \int_0^{\delta} 1 - \frac{v \cos\beta}{v_\infty \cos\beta_\infty} r dr \tag{2.6}$$

where v is the magnitude of the velocity in the defect region, r is the radial distance from the casing, and the subscript $()_\infty$ refers to the core stream.

The blockage calculated in the endwall module is as defined by Khalid (see Equation 1.2). For an axisymmetric flow with the defect at the casing, the relationship between the blockage and the streamwise displacement thickness can be expressed as

$$\frac{g}{c} \delta_{sw}^* = A_b, \tag{2.7}$$

where the streamwise displacement thickness is defined as

$$\delta^*_{sw} = \frac{1}{R_{cs}} \int_0^{\delta} 1 - \frac{v \cos(\beta_\infty - \beta)}{v_\infty} r dr. \tag{2.8}$$

The relationship between the momentum area and the streamwise momentum thickness can can similarly be expressed as

$$\frac{g}{c} \theta_{sw} = A_m, \tag{2.9}$$

where the streamwise momentum thickness is defined as

$$\theta_{sw} = \frac{1}{R_{cs}} \int_0^{\delta} \frac{v \cos(\beta_\infty - \beta)}{v_\infty} \left(1 - \frac{v \cos(\beta_\infty - \beta)}{v_\infty}\right) r dr. \tag{2.10}$$

Equations 2.6 and 2.8 are identical if the flow in the defect region has the same direction as the core, i.e. if $\beta = \beta_\infty$. However, this is not the case at the exit of a rotor, where the flow angle near the casing differs from the freestream. Therefore, assumptions have to be made about the radial profile of the velocity magnitude and direction in the endwall region in order to determine the AVDR from the blockage calculated in the endwall module. These assumptions are also necessary to characterize the transformation of apparent nonuniformity in velocity magnitude and direction between rotating and stationary frames.

The assumptions made regarding the variation of velocity magnitude and direction (viewed in the reference frame of the rotor) through the defect region are as follows:

- The flow angle at the casing, β_{wall}, is set equal to the angle of the tip clearance leakage flow at the trailing edge of the blade, based on observations from 3D RANS computations. The leakage angle flow calculation is described in Section 2.4.1.

- The flow angle varies linearly from the meanline value to the value at the casing over half the defect region.

$$\beta = \begin{cases} (\beta_\infty - \beta_{wall}) \frac{2r}{\delta} + \beta_{wall} & \text{if } r < .5\delta \\ \beta_\infty & \text{if } r \geq .5\delta \end{cases} \tag{2.11}$$

  This assumption stems from observations from set of RANS calculations by Lavainne[27].

- The magnitude of the velocity in the streamwise direction, $v_{sw} = v \cos(\beta - \beta_\infty)$, follows a power law for a turbulent boundary layer,

$$\frac{v_{sw}}{v_{\infty}} = \left(\frac{r}{\delta}\right)^{\frac{1}{n}}. \tag{2.12}$$

The radial extent of the defect, δ, and the shape of the profile, n, are set so that when Equation 2.12 is substituted into Equations 2.8 and 2.10, the blockage and momentum area from the calculations of leakage flow behavior are recovered.

Three parameters, δ_z^*, H, and β_{wall}, uniquely define the variation in the velocity vector though the endwall region under these conditions. The axial displacement thickness is calculated with Equation 2.6 using Equations 2.12 and 2.11 to define the velocity and angle in the defect region. The shape factor, H, is the ratio of the blockage to momentum area, A_b/A_m. Estimation of the flow angle at the casing, β_{wall}, is given in the list of assumptions above.

2.3.2 Endwall Loss

Assumptions about the extent of spanwise mixing are needed to determine the increase in entropy of the meanline flow due to loss in the endwall. The analogy of the wake in a pressure gradient includes a coupling between endwall and core flows. The entropy generation in these calculations is separate and implies that the flow in the meanline does not incur a total pressure loss due to losses in the endwall region. In other words, strict application of a wake-in-a-pressure-gradient blockage model would predict no effect of endwall losses on the total pressure outside of the defect region.

Previous researchers[1, 12, 13, 42], however, have shown that spanwise (radial) mixing in the blade row redistributes endwall losses, so the flow is not cleanly separated into inviscid and viscous regions. A method for estimating the effect of spanwise mixing on the specific entropy of the meanline flow is required.

Gallimore[12] investigated the effect of spanwise mixing using a streamline curvature calculation. The formulation allowed entropy to be added empirically to any given streamline. The model was used to investigate the entropy required to match the radial velocity distribution at the exit of a 4–stage research compressor with data from experiments. Calculation of the entropy distribution was performed for cases with and without spanwise mixing. The apparent loss distribution, for which no spanwise mixing was assumed, was then compared to the "actual" losses, for which spanwise mixing was present.

It was found that the redistribution of loss by mixing reduced the apparent endwall loss to nearly half the "actual" loss generated near the end walls, while the apparent meanline loss increased by around 50 percent over the expected profile loss. It is thus assumed here that streamwise mixing increases the entropy of the meanline flow over the profile losses by half the entropy generated in the endwalls. The effect of endwall loss on the meanline flow is input after the model has converged on a solution for AVDR.

2.4 Flow Feature Overview

This section describes flow features relevant to tip clearance blockage.

2.4.1 Leakage Jet

Two mechanisms cause fluid from the pressure side of a blade to move through the clearance gap to the suction side. The first is inviscid; the pressure difference across the blade tip drives fluid over the gap. The second is viscous. The relative motion of the casing wall tends to drag fluid through the gap. For clearances representative of those in modern compressors, the leakage flow over the clearance gap is primarily pressure driven[24].

Using this approximation, Storer[37] developed a method to predict the leakage angle of the flow exiting the suction side of the clearance gap. The flow was taken to be inviscid and incompressible, so leakage jet velocities on the pressure and suction sides of the clearance gap, v_{ps} and v_{ss} respectively, were determined from Bernoulli's equation

$$v_{ss} = \sqrt{\frac{2(P_t - P_{ps})}{\rho}} \qquad v_{ps} = \sqrt{\frac{2(P_t - P_{ps})}{\rho}}. \tag{2.13}$$

The pressure differences across and along the blade are of the same order of magnitude, but the thickness of a compressor blade is small compared to the chord. The pressure gradient across the clearance gap is therefore much greater than along the blade, allowing the assumption to be made that the leakage flow velocity component parallel to the blade does not change across the clearance gap. Given these conditions, the angle at which the leakage flow exits the suction side of the clearance gap, referenced to the chord of the blade,

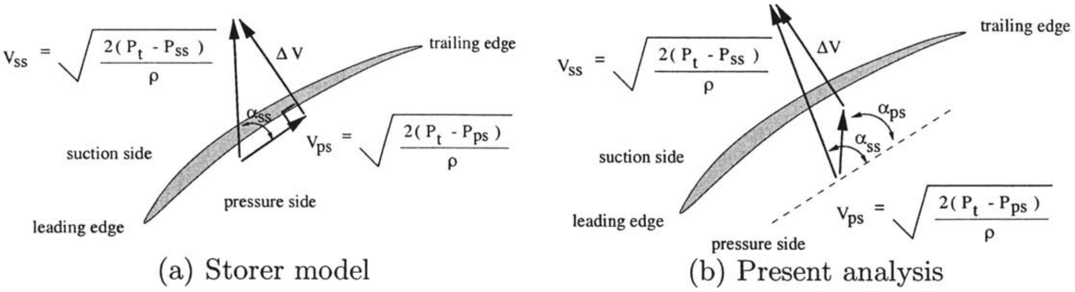

$V_{ss} = \sqrt{\frac{2(P_t - P_{ss})}{\rho}}$
ΔV
trailing edge
α_{ss}
$V_{ps} = \sqrt{\frac{2(P_t - P_{ps})}{\rho}}$
suction side
pressure side
leading edge
α_{ps}

(a) Storer model (b) Present analysis

Figure 2-2: Leakage Angle Calculation

is given by

$$\cos \alpha_{ss} = \cos \alpha_{ps} \sqrt{\frac{P_t - P_{ps}}{P_t - P_{ss}}}. \tag{2.14}$$

Storer assumed that near the pressure side, the clearance flow has no component of velocity in the direction normal to the blade surface as pictured in Figure 2-2(a). As will be shown in Section 2.6.2, however, that assumption can lead to underestimation of the suction side leakage angle, particularly when "double leakage" is present (see Section 2.4.3). Figure 2-2(b) shows this situation, in which the pressure side flow angle, α_{ps}, must be determined to calculate the suction side leakage angle, α_{ss}. A method for calculating the pressure side angle in the context of the current work is presented in Section 2.6.2.

2.4.2 Jet-Freestream Interaction

It is well known that tip leakage flow in a compressor rolls up into a vortex. This section focuses on the interaction of the leakage jet with the freestream prior to the roll up. Figure 2-3 shows tip clearance flow streamlines obtained from a 3D, steady, RANS calculation. The streamlines are marked approximately $1/20^{th}$ of a clearance gap away from the casing, but streamlines from other radial locations in the clearance gap show similar patterns. From the clearance gap of the lower blade in the figure, the streamlines are nearly straight and go across the passage. After some distance, the streamlines turn as they become part of a vortex. As seen in the figure, there is a distinct boundary that marks the penetration of the leakage flow into the main passage before the vortex roll up.

Khalsa[24] presented a modification of the theory of Martinez-Sanchez and Gauthier[31] to predict the trajectory of this boundary. The boundary was assumed to be a straight line intersecting the leading edge and inclined at an angle θ from the chord of the blade. The

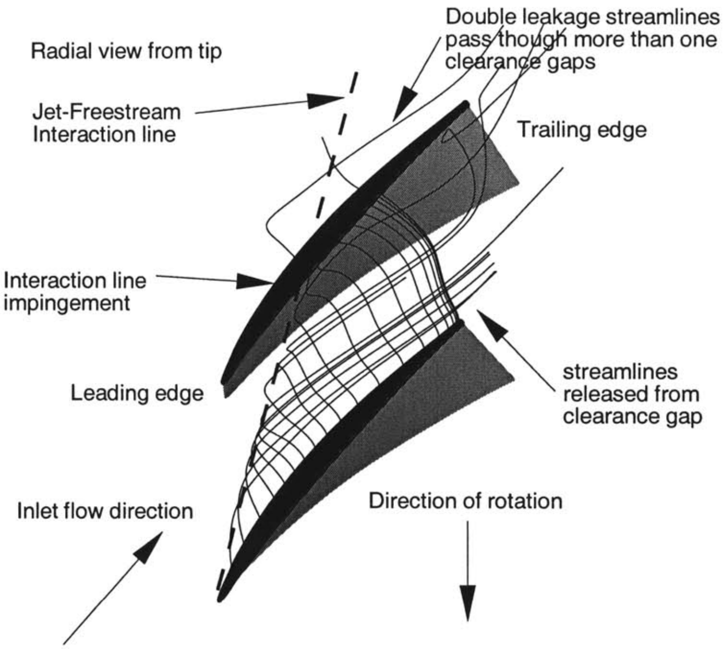
Radial view from tip
Jet-Freestream Interaction line
Double leakage streamlines pass though more than one clearance gaps
Trailing edge
Interaction line impingement
Leading edge
streamlines released from clearance gap
Inlet flow direction
Direction of rotation

Figure 2-3: Streamlines released from clearance gap

interaction between clearance jet and freestream was described using a constant pressure control volume, pictured in Figure 2-4. From conservation of momentum normal to the interaction line, θ can be calculated from the velocities of the two input streams and the angle of the leakage jet.

$$\tan\theta = \frac{\sin\alpha_{ss}}{(\frac{v_{fs}}{v_j}) + \cos\alpha_{ss}} \tag{2.15}$$

The velocities of the freestream and leakage jet, v_{fs} and v_j, are determined from the static pressure at the interaction point and the total pressure of each stream. Since v_{fs}/v_j and α_{ss} vary along the chord, the jet-freestream interaction line is taken as the average of θ along the chord.

2.4.3 Double Leakage and Clearance Gap P_t

The view taken by Martinez-Sanchez and Gauthier [31] and Storer and Cumpsty[38] was that the total pressure at the suction side of the clearance gap is the same as upstream of the blade row. However, the flow passing over the clearance gap subsequently mixes with the freestream. If a fluid particle that passes through the clearance gap passes through one

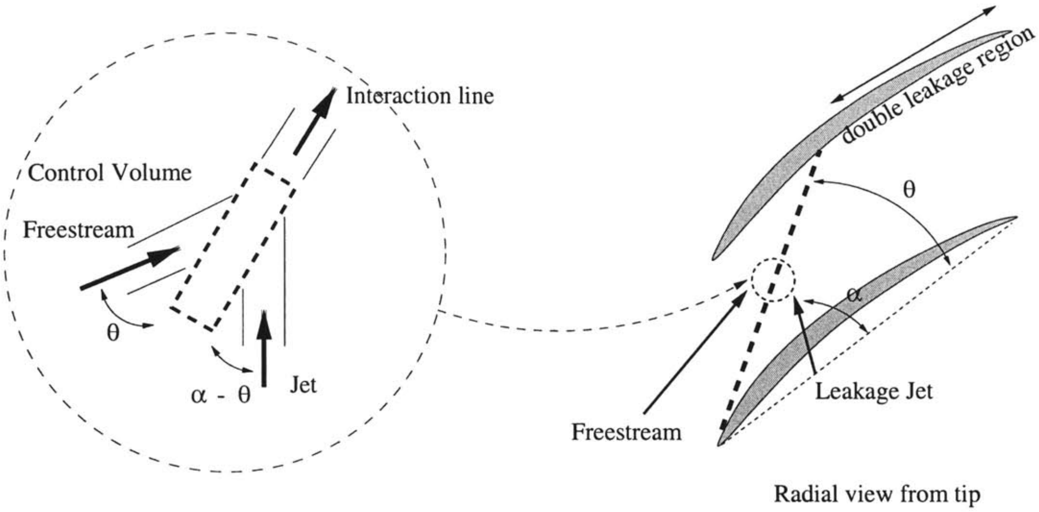

Figure 2-4: Interaction line control volume

or more additional clearance gaps, it will have lower total pressure than the freestream. This flow feature was first identified by Khalsa[24], who referred to it as "double leakage." The total pressure of the leakage flow at the suction side of the clearance gap is reduced in regions where double leakage occurs.

When the jet-freestream interaction boundary (Section 2.4.2) impinges on the pressure side of the next blade in the row, double leakage occurs downstream of the impingment point on that next blade. Double leakage can be seen in Figure 2-3. Upstream of the impingment, streamlines released from the clearance gap of the lower blade in the figure roll up into the clearance vortex before reaching the upper blade. Downstream of the impingment, the streamlines penetrate all the way across the passage and enter the clearance gap of the next blade .

The effect of double leakage is shown in Figure 2-5. The total pressure coefficient at the suction side of the clearance gap, $C_{p_t} = (\overline{P_t}^M - P_{t_1})/(P_{t_1} - P_1)$, where $\overline{P_t}^M$ is the radially mass averaged total pressure, is plotted as a function of chord. The computation shown is for the conditions of Figure 2-3. Downstream of the jet-interaction line impingment (which is near $x/c = 0.2$), the total pressure of the fluid exiting the clearance gap is substantially lower than in the freestream.

The calculation of double leakage given a specific geometry can readily be achieved through numerical simulation, but this approach is too computationally expensive for probabilistic analysis. What is required in the current model is a simple method for predicting

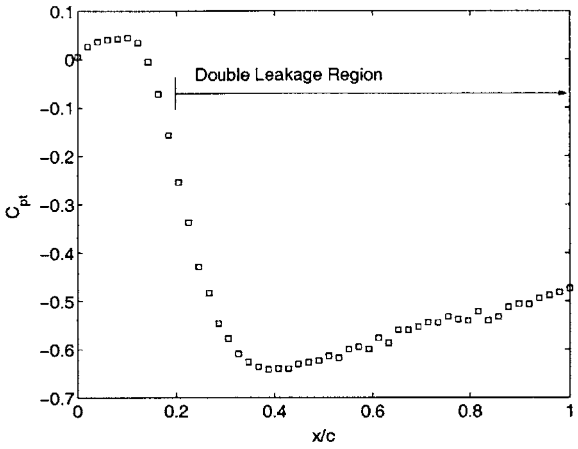

Figure 2-5: Reduction in $C_{p_t} = \frac{P_t - P_{t_1}}{P_{t_1} - P_1}$ due to double leakage

the magnitude of the total pressure loss associated with double leakage given the blade geometry and upstream flow conditions as inputs. Section 2.6.1 presents an empirical approach for estimating the total pressure in the clearance gap suitable for probabilistic analysis.

2.5 Tip Clearance Blockage Calculation

2.5.1 Calculation Overview

The tip clearance blockage model used in this thesis is a modified version of that proposed by Khalid et al.[23], based on the analogy between the development and growth of tip clearance blockage and a wake in a pressure gradient. In the analogy, the interaction between tip clearance flow and the freestream produces a velocity defect in the streamwise direction. As the defect travels toward the exit plane of the blade row, two competing effects determine the blockage development. The adverse pressure gradient in the passage causes the area and velocity defect of the wake to increase. Viscous effects tend to decrease the velocity defect. Khalid et al.[23] show that blockage models making use of this analogy follow trends seen in computations and in experiments.

To use this analogy, information needs to be provided about: i) the initial wake conditions (momentum and displacement thicknesses), ii) the pressure gradient, and iii) the rate of mixing between the defect and freestream. As Khalsa[24] notes, there are many ways to do this and the model used here is just one possible version.

The tip clearance flow is broken up along the chord into a number of individual leakage

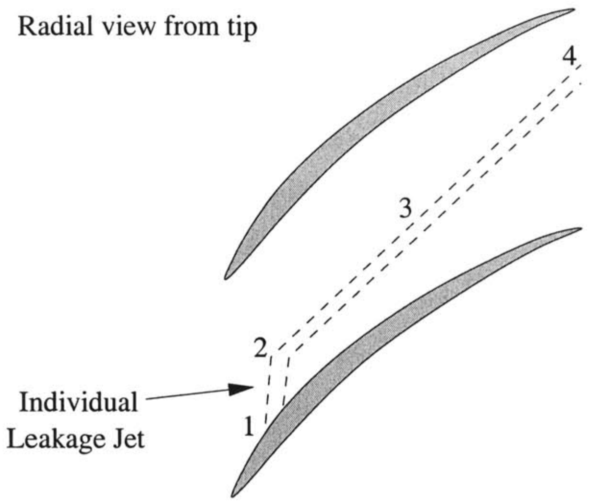

Figure 2-6: Blockage model diagram

jets which act independently, with the width of each leakage jet assumed constant. Several processes that happen simultaneously in reality are modeled as occurring in sequence. At the exit plane of the blade row, the blockages from each of the individual leakage jets are summed to produce the total blockage for the passage.

The sequence of flow processes is depicted in Figure 2-6.

1. The pressure difference from suction to pressure side drives fluid over the blade tip. The calculation of leakage jet velocity and flow angle was described in Section 2.4.1. Each individual leakage jet is assumed to be uniform in velocity and flow angle at the exit from the suction side of the clearance gap. The radial height of the jet at the clearance gap exit is equal to the height of the clearance gap vena contracta.

2. Near the suction side exit of the clearance gap, the leakage jet mixes with the freestream (Section 2.4.2). Conserving mass and momentum for the control volume pictured in Figure 2-4, the velocity and radial height of a uniform defect exiting the control volume can be calculated given the leakage jet angle and total pressure. The interaction is assumed to occur close enough to the clearance gap so the static pressure has the same value as Step 1. As noted in Section 2.4.3, the total pressure will be influenced by the presence of double leakage.

3. The defect progresses downstream, with the blockage growth modeled as a 2D turbulent wake in a pressure gradient and the mass and momentum defect specified by the

jet-freestream interaction in Step 2. The distance the flow travels is taken to be the straight line distance from the leakage jet point of origin on the suction side of the blade to the mid-passage location at the blade row exit plane. The static pressure at the exit of the passage is provided by the core flow module. Given the initial defect and pressure gradient, a set of ordinary differential equations for the wake is marched downstream to obtain the blockage and momentum area at the exit plane of the blade row. The width of the defect is assumed to be fixed, so all growth happens in the radial direction. Details of the wake calculation are given in Appendix A.

4. The final values for blockage and momentum area for each leakage jet are summed, defining the tip clearance blockage and momentum area for the passage.

2.5.2 New Developments in the Tip Clearance Model

Although the blockage model is based on the analogy with a wake in a pressure gradient, there are three differences with previous approaches. These are: i) the estimation of total pressure in the clearance gap, ii) the estimation of leakage angle, and iii) the calculation of a wake in a pressure gradient. These three differences are discussed next.

The blockage model in the paper by Khalid et al.[23] was implemented using computational results to define the total pressure in the clearance gap, which was an input to the calculation. However, in the framework of the present model, the total pressure in the clearance gap is not known apriori. A method is thus required to determine the total pressure in the clearance gap from upstream conditions, particularly in the presence of double leakage. That method is presented in Section 2.6.1.

The estimate of leakage angle used by Khalsa[24] and Storer and Cumpsty[38] assumes the clearance flow near the pressure side has no velocity normal to the blade. However, in double leakage regions, fluid particles pass over more than one clearance gap in the same blade row, implying there is such a normal velocity component. Section 2.6.2 shows that the normal velocity component should be accounted for (neglect of it gives an underestimation of leakage angle, and hence an underprediction of tip clearance blockage of roughly 50 percent). A method for estimating the normal velocity near the pressure side of the clearance gap is presented in Section 2.6.2.

The results described by Khalid et al.[23] were based on the wake in a pressure gradient calculation of Hill[18], where shape factor of the wake was assumed close to unity. Especially under highly loaded conditions, however, the shape factors of the initial defects specified by the control volume in Section 2.4.2 may be as large as 2.5. In this situation, the Hill model is not appropriate (it predicts smaller exit defects for larger inlet defects). A more general integral method[39] (described in Appendix A) was thus used.

2.6 Flow Feature Refinement

This section describes the determination of clearance gap total pressure and pressure side flow angle. The flow description is constructed from empirical observation. The data set used is a set of 3D RANS computations of a 3–stage compressor that were part of a sensitivity study reported by Lavainne[27]. The data include examination of the full compressor along a speed line at a nominal blade configuration, plus computations of the third stage along the same speed line with changes from the nominal configuration in tip clearance, chord, leading edge angle, trailing edge angle, and max thickness. Information about the geometric variation and operating conditions are given in [27].

From the computations, speedlines of three to eight points can be extracted from five distinct rotors, i.e. five rotors which each have a range operating conditions. These are rotor 1, rotor 2, rotor 3 with nominal tip clearances, rotor 3 with double tip clearance, and rotor 3 with half tip clearance. The five speedlines were used to define trends with loading and tip clearance.

2.6.1 Total Pressure Correlation

The total pressure in the clearance gap used in the present analysis has been correlated based on the computations just described. Figures 2-7(a)-(c) show clearance gap total pressure coefficient versus distance along the blade for different operating conditions. Blade rows with different ratios of tip clearance to chord, τ/c, are given in the different plots. The curves have similar characteristics in that the total pressure is close to the freestream value until the jet-freestream interaction boundary from the neighboring blade begins to impinge on its pressure side. At this location, the total pressure decreases. In the double leakage region, the tails of all the profiles on a given speed line collapse to nearly a single line for each τ/c.

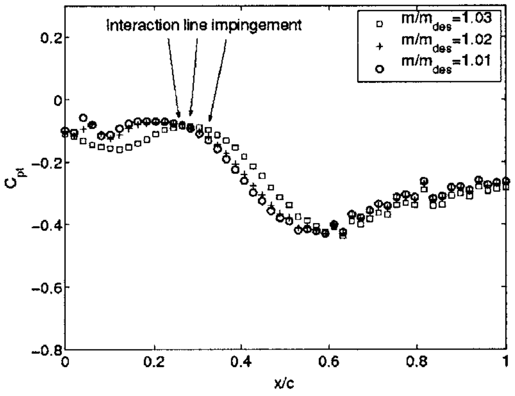

(a) Half the nominal tip clearance

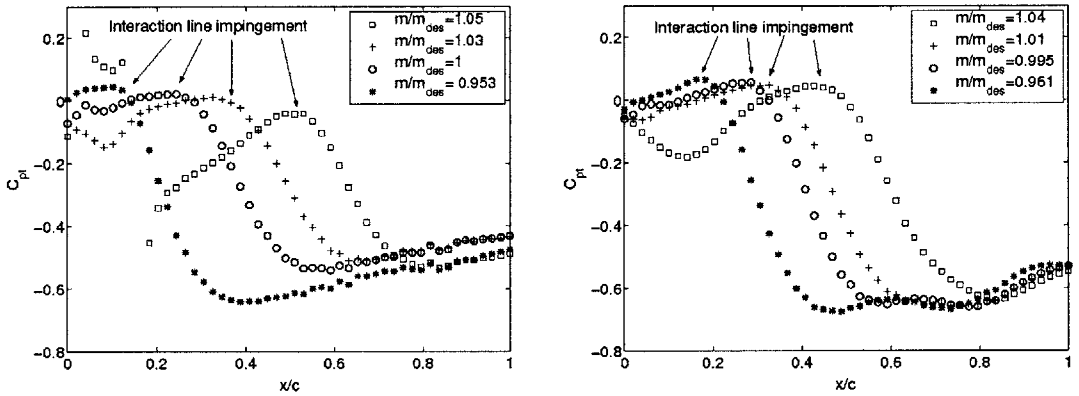

(b) Nominal tip clearance

(c) Double the nominal tip clearance

Figure 2-7: Contours of clearance gap $C_{p_t} = \frac{P_t - P_{t_1}}{P_{t_1} - P_1}$ from third stage 3D RANS computations with varying τ/c and $\dot{m}/\dot{m}_{design}$

A curve fit for the clearance gap total pressure profile is

$$C_{p_t} = (0.25\frac{x}{c} + 0.63e^{-89\tau/c} - 0.88)C_1(\frac{x}{c}) \tag{2.16}$$

where

$$C_1(\frac{x}{c}) = \begin{cases} 0 & \text{if } x < x_{dbl}, \\ .5\left[1 - \cos(\pi\frac{x - x_{dbl}}{0.25c})\right] & \text{if } x_{dbl} < x < x_{dbl} + 0.25c, \\ 1 & \text{if } x_{dbl} + 0.25c < x. \end{cases} \tag{2.17}$$

The location of the interaction boundary impingment, x_{dbl}, is found using the control volume analysis described in Section 2.4.2.

The leakage angle, α_{ss}, is an input to the control volume analysis, and is thus required to determine the total pressure profile. However, the total pressure distribution is required to determine the leakage angle, as seen in Equation 2.14. Therefore, the two quantities must be found iteratively. In the present model, this is done by guessing the location of the jet-freestream interaction impingment, x_{dbl}, finding the leakage angle using Equation 2.14, and using the total pressure and leakage angle profiles as inputs for the control volume analysis of Section 2.4.2. This determines the interaction boundary trajectory and gives a new value for x_{dbl}, which is used to update the old guess. The process is continued until the guess matches the calculated output.

2.6.2 Leakage Angle Refinement

To estimate the clearance flow leakage angle using Equation 2.14, the direction of the flow close to pressure side of the blade must be known because the assumption that the leakage flow is parallel to the blade on the pressure side is not appropriate in the presence of double leakage. Figure 2-8 shows the suction side leakage angle, α_{ss}, as a function of distance along the chord from 3D computations as well as α_{ss} based on the parallel flow approximation for the pressure side angle. The flow angle is underestimated over the rear half of the blade for both nominal and large tip clearances.

Underestimating the leakage angle affects both the calculation of the initial defect and the trajectory of the jet-freestream interaction boundary. Because the impingment location of the boundary is an input to the total pressure correlation of Section 2.6.1, the calculated total pressure variation along the chord is also affected. The result is an underestimate

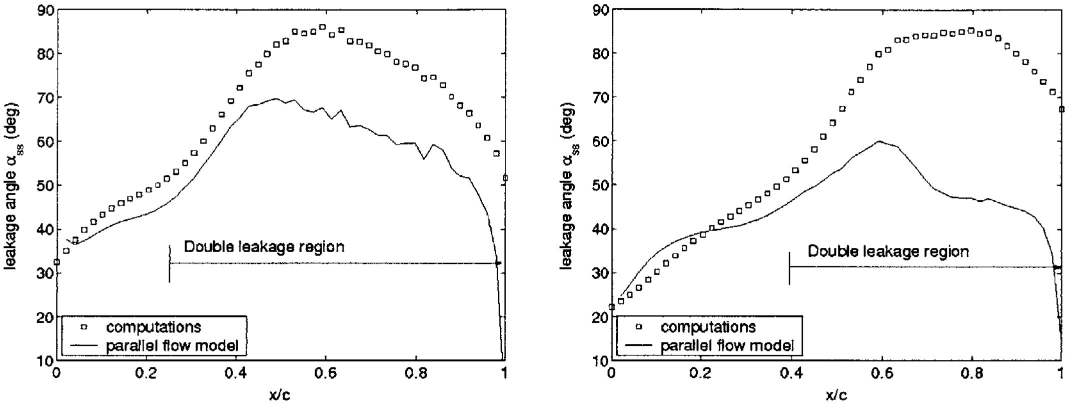

(a) nominal tip clearance (b) high tip clearance

Figure 2-8: Leakage angle model comparison

of tip clearance blockage. For the nominal tip clearance case shown in Figure 2-8(a), the blockage value computed using the parallel flow assumption is 59% lower than the value obtained using the leakage angle profile from the computation. For the high clearance case in Figure 2-8(b), the blockage is 52% lower using the parallel flow assumption.

α_{ps} Correlation

An estimate for the flow angle near the pressure side of the clearance gap is obtained from empirical correlation. The correlation is shown in Figures 2-9(a)-(c). It was observed that $\cos\alpha_{ps}$ is close to zero near the location on the chord where the jet-freestream interaction line impinges on the blade, x_{dbl}, after which $\cos\alpha_{ps}$ decreases. A minimum $\cos\alpha_{ps_{min}}$ is reached at x_{min}, and then $\cos\alpha_{ps}$ increases toward the trailing edge of the blade.

When $\cos\alpha_{ps}$ is nondimensionalized by $\cos\alpha_{ps_{min}}$ and the location on the chord is nondimensionalized by x_{dbl} and x_{min}, the data from the RANS computations collapse, as seen in Figure 2-9(a). The curve fit through the data is used in the model to estimate the variations of α_{ps} with x, the distance from the leading edge along the chord. Figures 2-9(b) and 2-9(c) define the correlations used to estimate x_{min} and $\cos\alpha_{ps_{min}}$ respectively.

2.7 Inlet Defect Evolution Calculation

This section estimates the contribution of nonuniformity, in inlet velocity magnitude and direction, on the blockage parameters at the exit. Like the tip clearance blockage, the model

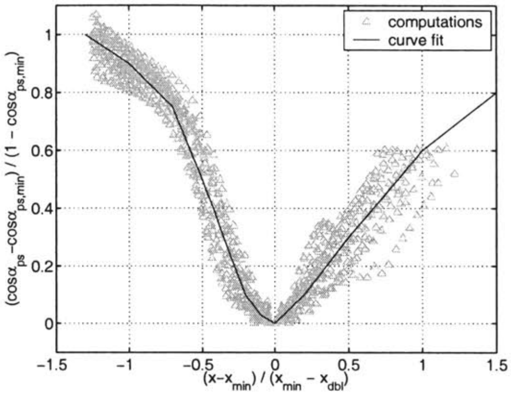

(a)

Variation of $cos\alpha_{ps}$ with chord. Several points along the chord are plotted for each computation.

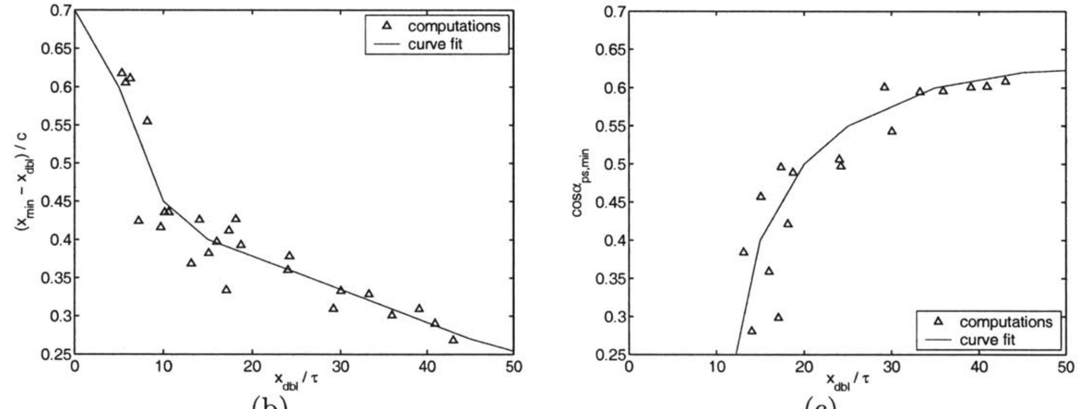

(b)

x_{min} as a function of x_{dbl}. Each point represent one computation.

(c)

$\cos\alpha_{ps_{min}}$ as a function of x_{dbl}. Each point represents one computation.

Figure 2-9: Pressure side leakage flow angle correlation

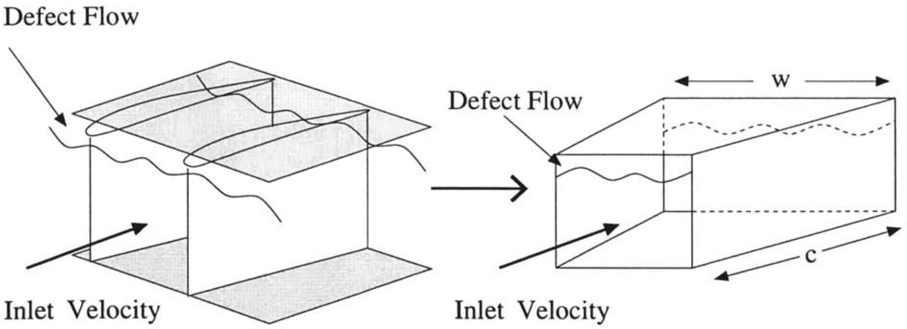

Figure 2-10: Diffuser Analogy

treats the defect as a wake in a pressure gradient. Given initial conditions of the defect, a integral wake calculation is performed to determine the blockage and momentum area at the exit plan of the blade row, as well as the entropy generated in the passage.

In this calculation the blade passage is treated as a diffuser, as pictured in Figure 2-10. The diffuser length is taken to be the chord of the blade. The variation in width of the diffuser along the streamwise direction is determined by solidity of the blade row and the meanline flow angle, $w = c\cos\beta/g$. The flow angle β is assumed to vary linearly between the upstream value of β_1, and the downstream value of β_2 that is determined by MISES. The height of the diffuser at the inlet is the blade passage height $h_1 = r_{cs_1} - r_{hub_1}$ and the height at the exit is taken as the blade passage height minus the streamwise displacement thickness generated by the tip clearance blockage, $h_2 = r_{cs_2} - r_{hub_2} - \delta^*_{sw,tip}$. The height is also assumed to vary linearly.

In the rotor frame of reference, the upstream defect flow may have a large variation in flow angle compared with the freestream, due to the change of reference between rotating and stationary frames, as pictured in Figure 2-11. In the figure, the flow coming from upstream is shown as collateral in the stationary frame (the defect flow has the same flow angle as the freestream)[1]. Due to the velocity difference between the two streams, however, the two streams differ in flow angle in the rotor frame of reference. The relative magnitude of the defect velocity compared to the freestream also changes.

The displacement and momentum thickness used in the diffuser analogy are based on a defect flow which is collateral with the freestream when it enters the blade passage. Because the upstream defect flow generally has a different flow angle compared with the freestream,

---

[1] This may not be the case in general.

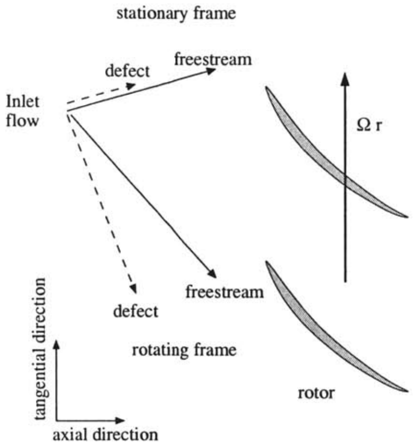

Figure 2-11: Defect skew due to shift of reference frames

it is assumed that the flow is inviscidly turned into the streamwise direction at the inlet of the diffusing passage. The calculation of the collateral defect parameters at the inlet of the diffusing passage from the upstream conditions is outlined below.

1. Axisymmetric profiles of velocity magnitude and direction from the upstream flow, described in Section 2.3.1, in the stationary frame of reference are used to calculate the profiles in the reference frame of the rotor. The flow will generally not be collateral in the rotating frame.

2. The axisymmetric velocity profile, $v(y)$, with the defect flow inviscidly turned into the streamwise direction in the reference frame of the current blade row is defined. This involves conservation of mass and conservation of total pressure along any streamline.

3. Displacement and momentum thicknesses are calculated using the collateral velocity profile, $v(y)$.

Given the inlet conditions, flow turning, and tip clearance effects, the evolution of the casing inlet defect through the diffuser can be calculated. The defect evolution in the streamwise direction, x, is described by a set of ordinary differential equations

$$\frac{1}{w\theta}\frac{\partial(w\theta)}{\partial x} + (H+2)\frac{1}{v_e}\frac{\partial v_e}{\partial x} = \frac{1}{w}\frac{\partial w}{\partial x} \tag{2.18}$$

$$\frac{H}{H^*}\frac{\partial H^*}{\partial H}\frac{1}{w\delta^*}\frac{\partial(w\delta^*)}{\partial x} - \frac{H}{H^*}\frac{\partial H^*}{\partial H}\frac{1}{w\theta}\frac{\partial(w\theta)}{\partial x} + (1-H)\frac{1}{v_e}\frac{\partial v_e}{\partial x} = \frac{2C_d}{\theta H^*} \tag{2.19}$$

$$\frac{1}{wh - w\delta^*}\frac{\partial(w\delta^*)}{\partial x} - \frac{1}{v_e}\frac{\partial v_e}{\partial x} = \frac{1}{wh - w\delta^*}\frac{\partial(wh)}{\partial x} \tag{2.20}$$

Equation 2.18 is the integral momentum equation for a wake when the width, w, is allowed to vary (see Figure 2-10). Equation 2.19 is a form of the kinetic energy integral equation. Equation 2.20 is the conservation of mass in the diffuser, providing coupling between the defect and freestream. The shape factor $H^* = \theta^*/\theta$ and the dissipation coefficient C_d are both functions of $H = \delta^*/\theta$, determined using the velocity profile of Hill et al.[18].

$$H^* = \frac{H^2 + 7H + 10}{9H}$$

$$C_d = K_p \frac{16\pi}{27} \frac{(H-1)^3}{H^3}$$

The development of these correlations, which are used in the tip clearance blockage model, is described in Appendix A.

The entropy generated by the wake, S_{gen}, is calculated from the dissipation coefficient.

$$C_d = \frac{T}{w\rho u_e^3}\frac{\delta S_{gen}}{\delta x} \tag{2.21}$$

Equations 2.18-2.20 and 2.21 are solved numerically given the inlet defect conditions using a Runge-Kutta solver. The values of displacement and momentum thickness at the end of the diffuser and the entropy generated are then used in the endwall module to determine the state of the endwall flow.

2.8 Assessment of Model Performance

Figure 2-12 compares axial displacement thickness from 3-stage compressor computations of Lavainne[27] to the blockage model presented in this chapter. The computation was conducted using the meanline blade profile and upstream flow conditions.

Figure 2-12(a) shows the comparison for the first rotor. The boundary layer has a displacement thickness of about 1% of the passage height at the inlet of the rotor which increases to around 3.25% at the exit. For the same inlet conditions, the model estimates a smaller downstream displacement thickness, on the order of 2.5% to 3%. However, the trend of the data with decreasing massflow (or increasing loading) is followed.

Figure 2-12(b) plots the comparison for the third stage rotor with nominal tip clearance.

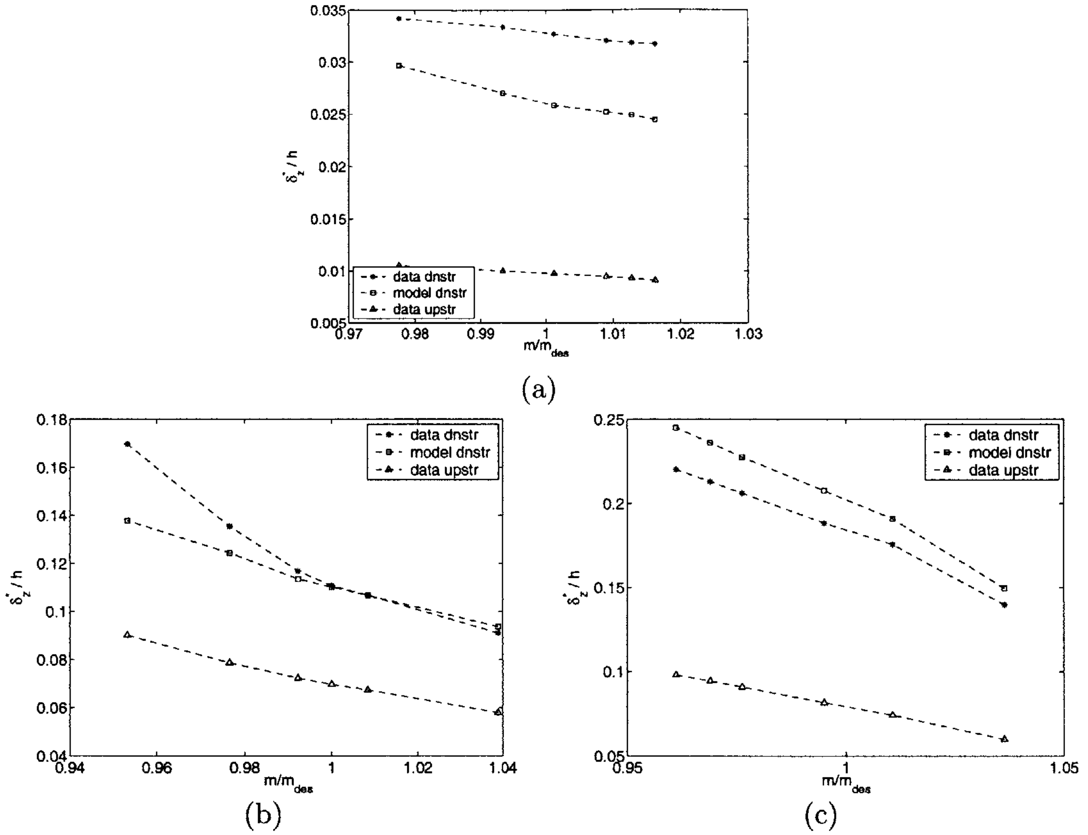

(a)

(b)

(c)

Figure 2-12: Blockage model comparison with data from Lavainne[27]

At higher massflows, model and data agree well. As the loading increases and the massflow decreases, the model begins to underestimate the displacement thickness, reaching a maximum error of 18% at the highest loading. The trend of increasing δ^*_z with increasing loading is still preserved.

Comparison for a third stage rotor with a tip clearance double that of the nominal geometry is plotted in Figure 2-12(c). For this case, the model overestimates the exit displacement thickness with an error on the order of 10% to 15%. However, as with the other rotor geometries, the trends in loading agree quite well. Further, the trend of increasing displacement thickness with increasing tip clearance is apparent in the model.

The empirical descriptions of total pressure in the clearance gap and flow angle near the pressure side of the clearance gap were both constructed using data from the RANS computations of Lavainne[27]. The assessment of the model performance in Figure 2-12 compares the model with those same computations. Thus, the figure is not showing an independent calculation of blockage, but rather that the model is consistent with the calculations. The ability of the model to predict the blockage for a generic rotor configuration is yet untested. However, previous versions of wake-in-a-pressure-gradient blockage models have been shown to follow trends seen in computations and experiments[23], so the consistency check provided by Figure 2-12 gives some assurance that the model is applicable to trends seen in generic rotors. In summary, the ability of the model to follow the trends gives support that it is a useful tool for preliminary investigations and, for the present work, suitable for probabilistic analysis.

2.9 Chapter Summary

This chapter presented a meanline model to be used in the probabilistic analysis of a compressor rotor. The model couples a core flow and endwall module, the latter providing a description of tip clearance blockage and loss. The blockage model is derived from that of Khalsa[24], using analogy with a wake in a pressure gradient, but empirical information is added to account for the effects of double leakage on the tip clearance flow. The model is compared to 3D RANS computations to show that trends with loading and tip clearance concur.

Chapter 3

Analytical Framework and Probabilistic Approach

This chapter describes the framework used to conduct the probabilistic analysis of rotor performance, including the nominal and probabilistic performance metrics examined and the tools used in the probabilistic analysis.

3.1 Rotor Geometry

The blade row used in the study is a low speed rotor with double circular arc (DCA) blading modeled after the GE E3 Rotor B, described by Wisler[41]. The passage and blade geometry are listed in Table 3.1 and the velocity triangle specification is given in Table 3.2. The geometry definition is diagrammed in Figure 3-1. The geometry was chosen to mimic the later stages of a high pressure compressor, where the small annulus height and low aspect ratio heighten the importance of tip clearance effects.

Small changes were made to the meanline geometry of Rotor B to simplify the probabilistic analysis. A DCA airfoil (see Cumpsty[5]) replaces Rotor B's modified DCA airfoil, simplifying the construction of the blade shape from a given sample of blade parameters. The change in profile affects the blade turning for given leading and trailing edge angles, so the trailing edge angle was modified to preserve Rotor B's velocity triangles at the design condition. All other aspects of the geometry used in this thesis are the same as for Rotor B.

Table 3.1: Geometry Specification

Parameter	Dimension
casing radius	76.2 cm
hub radius	64.8 cm
chord	9.6 cm
tip clearance	0.02 c
solidity	1.16
β_1	68.4 deg
β_2	34.0 deg
t_{max}	0.06 c
R_{le}	0.1 t_{max}

Table 3.2: Design Velocity Triangle Specifications

	rotor inlet	rotor exit
wheel speed (m/s)	53.3	53.3
V'_θ (m/s)	44.6	26.2
V_z (m/s)	26.3	27.0
β' (deg)	59.5	44.1
α (deg)	18.4	45.1

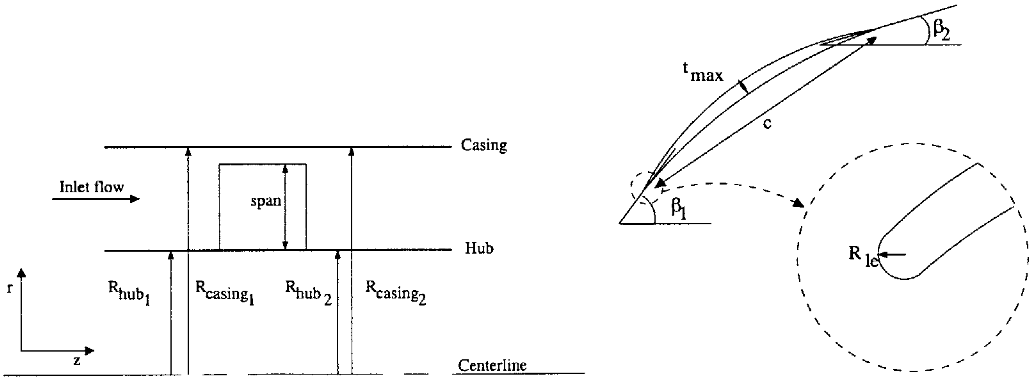
Casing
Inlet flow
span
Hub
r
z
R_{hub_1}
R_{casing_1}
R_{hub_2}
R_{casing_2}
Centerline
t_{max}
c
β_2
β_1
R_{le}

(a)
Meridional dimensions

(b)
Blade profile dimensions

Figure 3-1: Rotor geometry dimensions

Table 3.3: Rotor nominal performance

	design	near stall
ϕ	0.49	0.325
C_p	.432	.595
ω	0.057	0.13
α_2 (deg)	45.1	58.6
δ_z^*/h	0.047	0.14
ψ_{stall}	0.223	0.223

3.1.1 Nominal Performance

The nominal performance of the compressor at a given flow coefficient, $\phi = v_z/U$, will be described here by the following parameters:

- static pressure rise, $C_p = \frac{P_2 - P_1}{P_{t_1} - P_1}$
- loss, $\overline{\omega} = \frac{\overline{P_{t_2}}^m - P_{t_1}}{P_{t_1} - P_1}$, where $\overline{P_{t_2}}^m$ is the mass averaged total pressure at the exit of the blade row. This is the measure of blade row efficiency.
- stalling total-to-static pressure rise, $\psi_{stall} = \frac{P_{stall} - P_{t_1}}{\rho U^2}$
- exit flow angle (in the stationary frame of reference), α_2
- exit axial displacement thickness, δ_z^*

Pressure rise, loss, and stalling pressure rise are typical performance metrics for a blade row. Exit flow angle and displacement thickness are also included because of their impact on matching between blade rows. Variations in these quantities at the exit of the rotor affect the performance of the downstream stator by changing the effective incidence angle at the meanline and the degree of skew near the endwall. Therefore, in the context of a multistage machine, these two are also important metrics. The nominal performance[1] for design and near stall flow coefficients are listed in Table 3.3.

The stall point is taken as the peak of the total-to-static characteristic of the rotor,

$$\frac{\partial}{\partial \phi}\left(\frac{P_2 - P_{t_1}}{\rho U^2}\right) = 0. \tag{3.1}$$

---

[1] Nominal performance is defined as the deterministic performance attained when all inlet variables are at their intended design values.

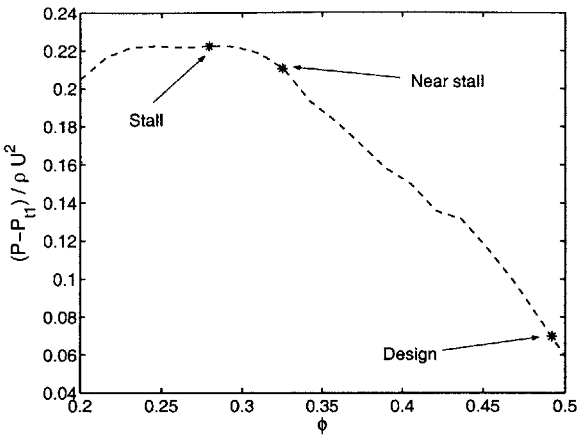

Figure 3-2: Rotor total-to-static characteristic

This approximation of the stall point comes from two-dimensional stability theory, which predicts the conditions in which modal instabilities can grow into rotating stall[5]. It is recognized that there are other routes to stall[16]; these are not addressed. The goal here is to understand the effect of geometric variability on peak pressure rise, not investigate in-depth the inception of rotating stall. Thus, for purpose of this thesis, a simple description will suffice.

The characteristic for the current rotor for the nominal geometry is shown in Figure 3-2. Stall occurs at a flow coefficient of $\phi = 0.28$ and a pressure rise of $\psi_{stall} = 0.22$. In the probabilistic simulations, the stalling pressure rise is found by performing computations for decreasing flow coefficients until the slope of the total-to-static characteristic becomes positive. A cubic spline of the points surveyed is created, and the stalling condition is taken to be the peak of the curve created by that spline.

3.2 Variability Quantification

This section describes the variability in the rotor geometric parameters and the quantification of the resulting variations in performance.

3.2.1 Geometric Variability

The variability in the geometry of the rotor is described by assigning uncertainty to the key geometric parameters according to typical manufacturing tolerances. For a dimension

Table 3.4: Rotor Geometric variability

parameter	mean	2σ variation
hub radius	67.8 cm	0.01% R_{hub}
casing radius	76.2 cm	0.01% R_{casing}
blade span	11.2 cm	0.2% b
max blade thickness	0.06 c	0.5% c
leading edge radius	0.1 t_{max}	0.1% c
leading edge angle	68.4 deg	0.42 deg
trailing edge angle	34.0 deg	0.42 deg

specified as $p \pm q$, p is taken to be the mean and q is taken as a two standard deviation variation from the mean. The level of variability for each parameter is listed in Table 3.4. The parameters listed are taken as mutually independent and normally distributed. The chord length is not included in the list, as previous studies have shown that typical variations in chord do not make a significant impact on the variability in rotor performance[27]. The levels of variability are taken from Lavainne[27] and Dong[7].

3.2.2 Performance Variability

In this thesis, the probabilistic performance of a rotor is measured by the following parameters, diagrammed in Figure 3-3:

- The mean shift, defined as the difference between the the nominal performance, when all inputs are taken at their design value, and the mean performance. Mean shifts can occur when at least one of the input distributions are not symmetric about their mean, or when the output is a nonlinear function of the inputs.

- The standard deviation, which measures the spread of the output population.

- The 5^{th} and 95^{th} quantiles, defined as the values at which the cumulated distribution function reaches 0.05 and 0.95, respectively. 90% of the rotors will have a performance that falls within this range. The distances between each quantile and the mean also give an indication of the symmetry of the output distribution.

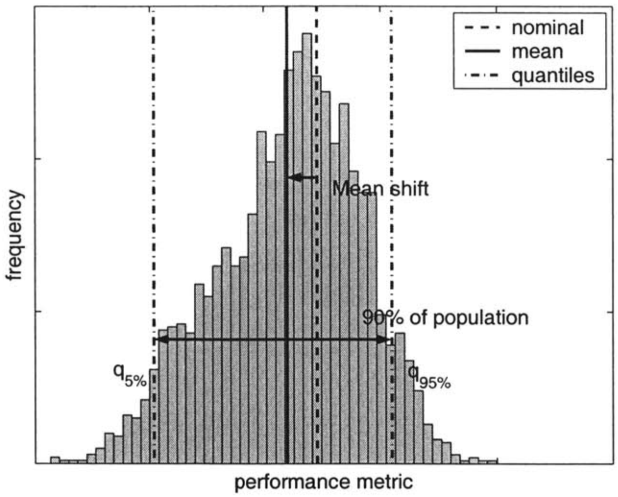

Figure 3-3: Illustration of probabilistic performance metrics

3.3 Monte Carlo Simulation

The probabilistic performance metrics defined in Section 3.2.2 are evaluated from the meanline model using Monte Carlo simulation. Monte Carlo methods are numerical techniques for evaluating multivariate integrals by random quadrature[11]. They are similar to Simpson's Rule or trapezoidal integration of single variate integrals, where an approximation to an integral is obtained by determining the value of the integrand for select values of the independent variable. In Monte Carlo, the values of the independent variables are obtained by random sampling. The method can be applied to any multivariate integral and is particularly useful when an analytic solution does not exist.

In the current context, Monte Carlo simulation is used to estimate the probabilistic moments used to describe the rotor performance variability. A random sample is drawn from each rotor geometric parameter according to its probability density function (PDF). The vector containing these parameters, X_i, represents one possible rotor configuration for the given tolerances. This geometry is simulated in the meanline model, and the corresponding performance metric Y_i is obtained. This process is repeated, creating a set of performance samples Y for geometries X. Each Y_i is similar to an experimental observation of the system and therefore can be treated statistically. The set of samples Y_i can be used to build empirical PDF's of the performance metrics, allowing the variability to be quantified.

As the number of samples becomes large, Monte Carlo methods can be proven to asymptote to exact solutions[11]. However for a finite sample size, the solution will be uncertain, the amount of uncertainty increasing as the sample size decreases. The metrics for the quantification of variability, such as the mean and standard deviation, are therefore random variables themselves with variance that decreases to zero as the sample size increases. The lower the variance, the more accurate the solution. Variance of the solution is affected by the system simulated, the number of simulations, and the scheme used to generate input samples. In cases where individual simulations are computationally expensive, there exist a number of sampling schemes that can reduce the variance for a given number of total simulations, one of which is described below.

3.3.1 Repeated Latin Hypercube Sampling

The basic Monte Carlo sampling scheme is known as simple random sampling (SRS), where each sample is chosen randomly from the joint PDF of X. Latin hypercube sampling (LHS) is another sampling scheme which can reduce the variance of the output metrics for a given sample size. LHS samples have a variance that is no larger than SRS, and depending on the characteristics of the function simulated, the variance can be greatly reduced[11]. Stein[36] shows that LHS takes advantage of linearities in the function to reduce the variance and for highly non-linear functions may not provide significant variance reduction over SRS (Manteufel[30]). However, in the present work, the cost to generate the samples is negligible compared to the cost of the simulations themselves, so the opportunity for variance reduction makes LHS attractive.

Latin hypercube samples are constructed by discretizing the PDF of each input variable into M bins of equal probability. For a K dimensional parameter space, there will be M^K possible bins. Then, M random samples are generated such that every variable has one sample in each of its M bins. This is illustrated for two variables in Figure 3-4. (For $M = 1$, LHS is equivalent to SRS). All M samples in an LHS set must be simulated in order for the output variability to be properly estimated.

Owen[34] showed that estimates of probabilistic moments from LHS sets follow the central limit theorem; for large M, estimates of a variability metric x coming from repeated Latin hypercube sample sets appear as if sampled from a normal distribution. This allows

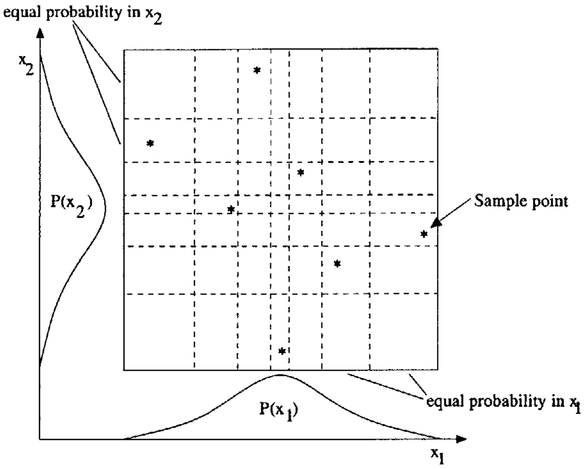

Figure 3-4: Latin hypercube sample construction

the confidence interval for the estimate to be found by classical interval estimation[2],

$$\langle\mu\rangle_{1-\alpha} = \left(\overline{x} - t_{\alpha/2,N-1}\frac{s}{\sqrt{N}}, \overline{x} + t_{\alpha/2,N-1}\frac{s}{\sqrt{N}}\right), \tag{3.2}$$

where $\langle\mu\rangle_{1-\alpha}$ is the $1-\alpha$ confidence interval for the performance metric, N is the number of LHS sample sets, $\overline{x}$ is the sample mean of x from the N sets, s is the sample standard deviation of x from the N sets, and $1-\alpha$ is the confidence. $t_{\alpha/2,N-1}$ is value of the inverse CDF of the Student's t-distribution with $N-1$ degrees of freedom, evaluated at $\alpha/2$. Equation 3.2 states that if the analysis were repeated many times, $1-\alpha$ of the solutions from the analysis (a typical value quoted is 95%) would be between $\overline{x} - t_{\alpha/2,N-1}\frac{s}{\sqrt{N}}$ and $\overline{x} + t_{\alpha/2,N-1}\frac{s}{\sqrt{N}}$.

3.3.2 Response Surface Modeling

Monte Carlo simulation with Latin hypercube sampling can produce low enough variance estimates to distinguish variability drivers of rotor performance in on the order of a few thousand iterations. The meanline model presented in Chapter 2 may take on the order of 20 minutes per simulation on a 1.5 GHz computer, including the extra simulations needed to determine the stalling pressure rise. Taking advantage of the parallel computing inherent in MCS, a single design point or near stall probabilistic analysis is thus tractable. To define the main drivers of variability, however, it is necessary to conduct a parametric study of input variability which requires more sets of Monte Carlo runs. With the current model and computational power, such an analysis is still too expensive to conduct with MCS alone.

To find the key drivers of variability, a "meta-model" of the meanline model is built for each performance metric that allows the effect of variability from each input parameter to estimated rapidly. A response surface is built by fitting the performance metrics from 20 of the LHS sets to a second order polynomial of the form

$$y = a_0 + x^T a + x^T B x. \tag{3.3}$$

Here, x is a vector of the input geometric dimensions of the rotor, and y is the corresponding performance. The vector a contains the coefficients of the linear terms and the matrix B contains the coefficients to quadratic terms.

MCS can be performed on the response surface with very little computational cost, allowing rapid comparisons of the impact of the different variability sources.

3.4 Chapter Summary

This chapter outlined the analytical framework and analysis tools (Monte Carlo simulation and Latin hypercube sampling) used to conduct the probabilistic analysis of a compressor rotor. The effect of the independent normally distributed input variables will be assessed by measuring the mean shift, standard deviation, and 5% and 95% quantiles of the output probabilistic distributions. To limit computational costs, a response surface model was built for accessing parametric sensitivity of inlet variability.

Chapter 4

Analysis Results

This chapter presents the results of the probabilistic analysis of compressor rotor performance. Performance variability at design and near stall, given rotor geometric variability, is quantified and the key drivers of variability at each condition are assessed.

4.1 Variability Characterization

The Monte Carlo analysis performed on the full meanline model for both design and near–stall flow coefficients contained 49 LHS sets with 50 bins per set, a total of 2450 simulations at each condition. Histograms of the output performance are shown in Figure 4-1 for the design condition and in Figure 4-2 for the near-stall condition. The results are tabulated in Table 4.1 for the design condition and in Table 4.2 for near-stall. The results for stalling pressure rise are included with the design condition data.

The mean shifts are generally small at design; the static pressure coefficient and exit angle show no appreciable mean shift. The mean of the displacement thickness and loss shift +0.6% and +0.4% from their respective nominal values. Closer to stall, the mean shifts of the static pressure coefficient and exit angle are -0.4% of nominal and -0.05 degrees respectively. The axial displacement thickness mean shifts -2.2% of the nominal value and the loss shifts 0.6%. The mean of the peak total-to-static coefficient is 0.8% higher than the nominal.

The standard deviations for the two conditions are compared using the coefficient of variation (COV), σ/μ. The COV is relatively unchanged between the two conditions, as seen in the rightmost columns of Tables 4.1 and 4.2.

Table 4.1: On–design performance variability
± represents the bounds of a 95% confidence interval

	nominal	μ	σ	$Q_{5\%}$	$Q_{95\%}$	COV
C_p	0.432	0.432 $\pm 1.7 \times 10^{-5}$	0.00480 $\pm 1.1 \times 10^{-4}$	0.424 $\pm 3.6 \times 10^{-4}$	0.439 $\pm 2.9 \times 10^{-4}$	1.1%
ω	0.0570	0.0573 $\pm 9.1 \times 10^{-6}$	0.00186 $\pm 4.5 \times 10^{-5}$	0.0541 $\pm 1.2 \times 10^{-4}$	0.0602 $\pm 1.3 \times 10^{-4}$	3.3%
δ_z^*/h_{nom}	0.0466	0.0469 $\pm 1.1 \times 10^{-5}$	0.00232 $\pm 4.4 \times 10^{-5}$	0.0428 $\pm 1.2 \times 10^{-4}$	0.0504 $\pm 1.1 \times 10^{-4}$	5.0%
α_2 (deg)	45.1	45.1 $\pm 7.8 \times 10^{-4}$	0.211 $\pm 4.7 \times 10^{-3}$	44.7 ± 0.016	45.4 ± 0.012	0.5%
ψ_{stall}	0.223	0.224 $\pm 2.9 \times 10^{-5}$	0.00255 $\pm 6.7 \times 10^{-5}$	0.220 $\pm 1.7 \times 10^{-4}$	0.228 $\pm 1.5 \times 10^{-4}$	1.1%

Table 4.2: Near–stall performance variability
± represents the bounds of a 95% confidence interval

	nominal	μ	σ	$Q_{5\%}$	$Q_{95\%}$	COV
C_p	0.595	0.592 $\pm 8.2 \times 10^{-5}$	0.00627 $\pm 1.5 \times 10^{-4}$	0.580 $\pm 3.9 \times 10^{-4}$	0.601 $\pm 3.1 \times 10^{-4}$	1.1%
ω	0.129	0.128 $\pm 4.5 \times 10^{-5}$	0.00372 $\pm 8.1 \times 10^{-5}$	0.122 $\pm 2.6 \times 10^{-4}$	0.134 $\pm 2.1 \times 10^{-4}$	2.9%
δ_z^*/h_{nom}	0.135	0.132 $\pm 6.1 \times 10^{-5}$	0.00499 $\pm 9.4 \times 10^{-5}$	0.123 $\pm 3.9 \times 10^{-4}$	0.140 $\pm 2.3 \times 10^{-4}$	3.8%
α_2 (deg)	58.6	58.5 ± 0.00401	0.332 ± 0.00879	57.8 ± 0.0231	58.9 ± 0.0191	0.6%

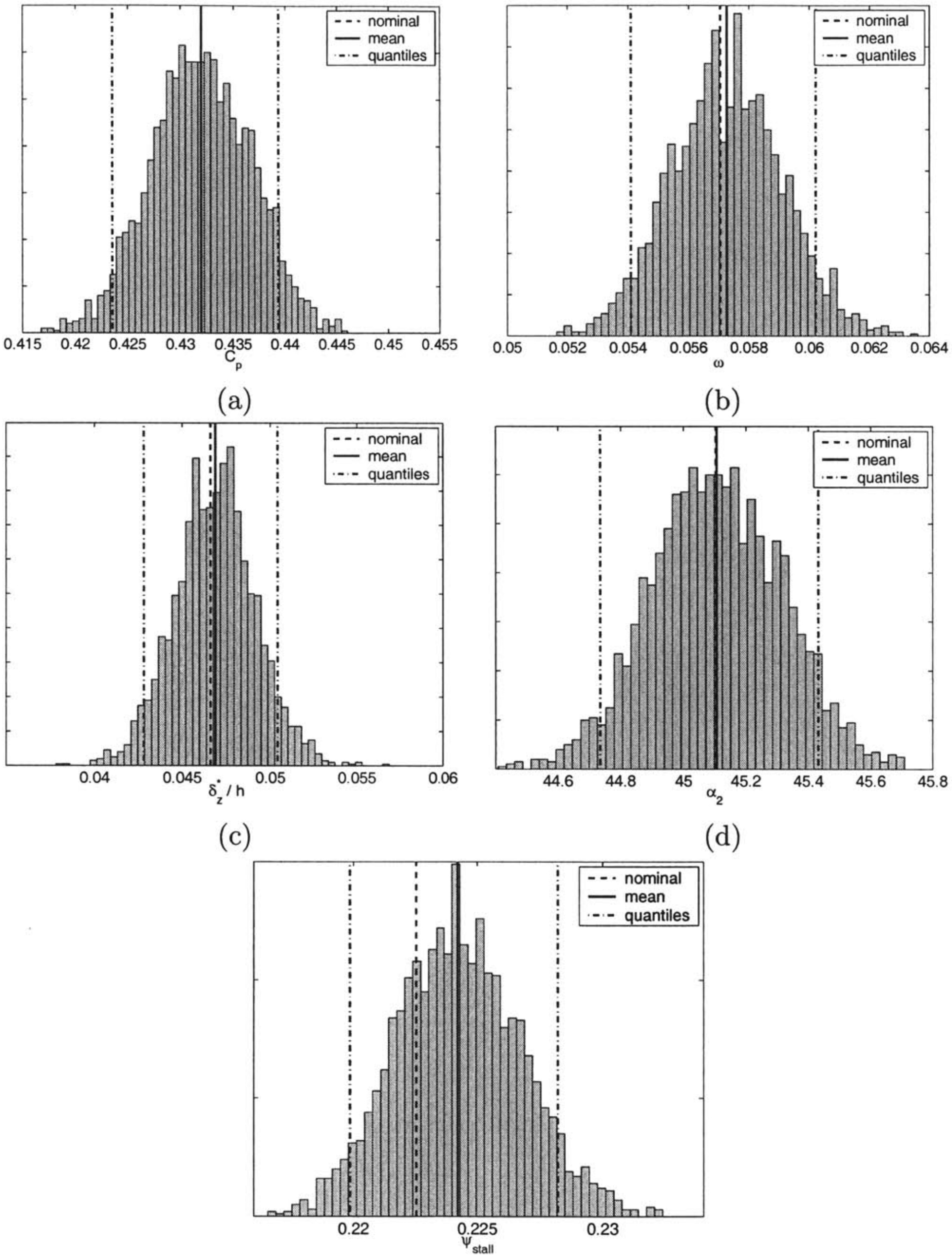

(a) (b) (c) (d) (e)

Figure 4-1: On–design performance variability

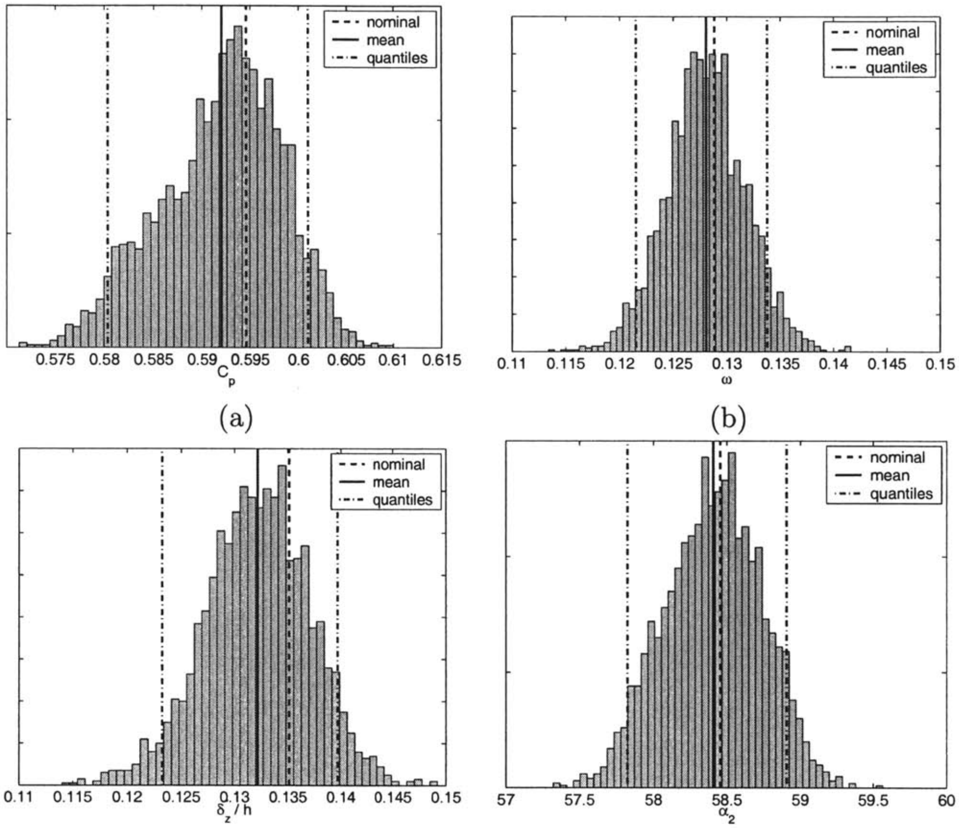

(a) (b)

(c) (d)

Figure 4-2: Near–stall performance variability

The 5% and 95% quantiles indicate that 90% of rotors with the given amount of geometric variability will have a pressure rise coefficient between 0.424 and 0.439, a range of 0.016, at design. The range of values for loss, δ_z^*/h_{nom}, and exit angle at the design condition are 0.0061, 0.074, and 0.68 degrees respectively. Near stall, those ranges become 0.012, 0.047, and 1.1 degrees respectively. The range in pressure rise coefficient is 0.021 near stall and the ψ_{max} as a range of 0.0084.

For all the metrics shown, the mean is essentially centered between the 5% and 95% quantiles. For the design cases, the ratio $(\mu - Q_{5\%})/(Q_{95\%} - Q_{5\%})$ is 0.54, 0.52, 0.53, and 0.53 for the pressure rise coefficient, loss coefficient, displacement thickness, and exit angle respectively. Close to stall, the ratios for the performance metrics are 0.57, 0.53, 0.54, and 0.53, in the same order. For the stalling pressure rise, $(\mu - Q_{5\%})/(Q_{95\%} - Q_{5\%})$ is equal to 0.52.

4.2 Assessment of the Key Drivers of Variability

This section identifies the key drivers of variability among the input geometric noises. The variation in each performance metric is calculated with one of the noise parameters held fixed at its nominal value. The influence of that metric on the variability in performance is then inferred by comparing the change in variability when all parameters are allowed to vary.

As noted in Section 3.3.2, the meanline model of Chapter 2 is too computationally intensive for the repeated probabilistic analyses needed for a parametric study. Therefore, a quadratic response surface is used in place of the meanline model in the assessment of variability. The response surfaces were constructed using data from 20 LHS sets, finding the least squares solution to the polynomial coefficients in Equation 3.3. Probabilistic analyses using the response surface were run using 100 LHS sets of 1000 bins per set, totaling 100,000 simulations per analysis.

4.2.1 RSM Fit Assessment

This section examines the extent which the response surface model captures the variability of the full meanline model. Figures 4-3 and 4-4 compare the empirical PDF's generated from the meanline model and the response surface for each output variable. The comparison

Table 4.3: RSM on–design performance variability

	μ	σ	$Q_{5\%}$	$Q_{95\%}$	COV
C_p	0.432	0.00479	0.4241	0.440	1.1%
ω	0.0572	0.00183	0.0542	0.0602	3.2%
δ_z^*/h_{nom}	0.0469	0.00228	0.0431	0.0506	4.8%
α_2 (deg)	45.1	0.21	44.8	45.4	0.5%
ψ_{stall}	0.224	0.00227	0.221	0.228	1.0%

Table 4.4: RSM near–stall performance variability

	μ	σ	$Q_{5\%}$	$Q_{95\%}$	COV
C_p	0.592	0.00444	0.585	0.599	0.7%
ω	0.128	0.00342	0.122	0.134	2.7%
δ_z^*/h_{nom}	0.132	0.00473	0.124	0.140	3.6%
α_2	58.4	0.28	58.0	58.9	0.5%

of cumulative distribution function (CDF) appears in Appendix B. Tables 4.3 and 4.4 list the probabilistic metrics as calculated by the response surface, to be compared to Tables 4.1 and 4.2 from the meanline model.

As seen in Figures 4-3(a)-(d), the response surface mimics the probabilistic distribution seen in the meanline model at design. A comparison between Tables 4.1 and 4.3 shows that the difference in mean between the two models is less than 0.2%. The difference in variance is less than 2% for all metrics.

The response surface method does a worse job of representing the meanline model at the near-stall condition. The PDF's for loss and δ_z^*/h_{nom} shown in Figures 4-4(b) and (c) agree well. However, Figures 4-4(a), and (d) representing the pressure rise coefficient and exit angle, show departures from the meanline PDF. In those cases, the probability in the lower tail of the RSM distribution is smaller that that of the meanline. A comparison between Tables 4.2 and 4.4 shows that the response surface underestimates the standard deviation of the pressure rise and exit angle by 29.2% and 15.7% respectively, due to the inability of the response surface to capture the tails of the distribution. The shape of the distribution closer to the mean is better matched. Although the response surface model does not match the meanline variability exactly, the ability to capture the variability near the mean should still be sufficient to determine which drivers are most responsible for performance variability.

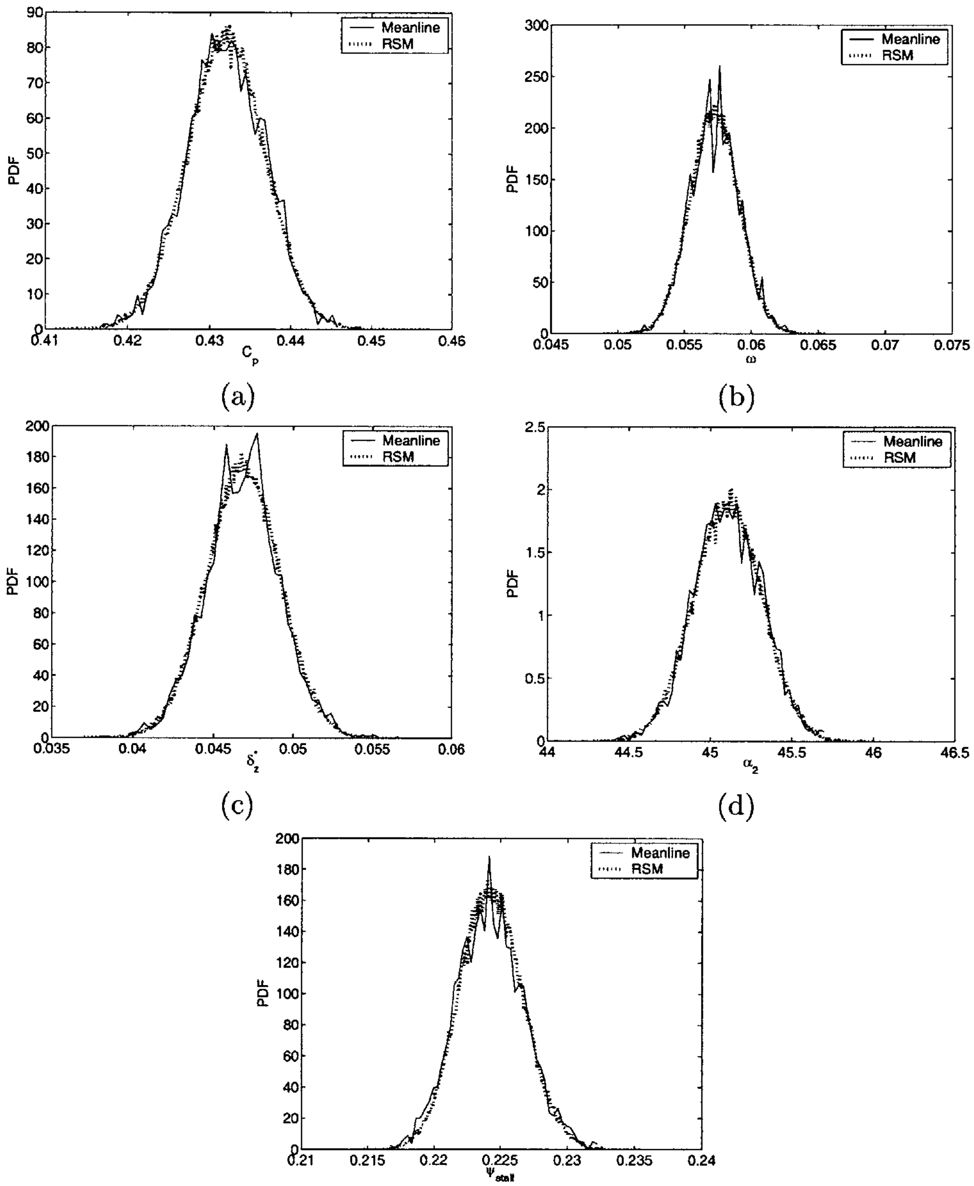

(a) (b)

(c) (d)

(e)

Figure 4-3: Response surface method (RSM) vs. model for design conditions

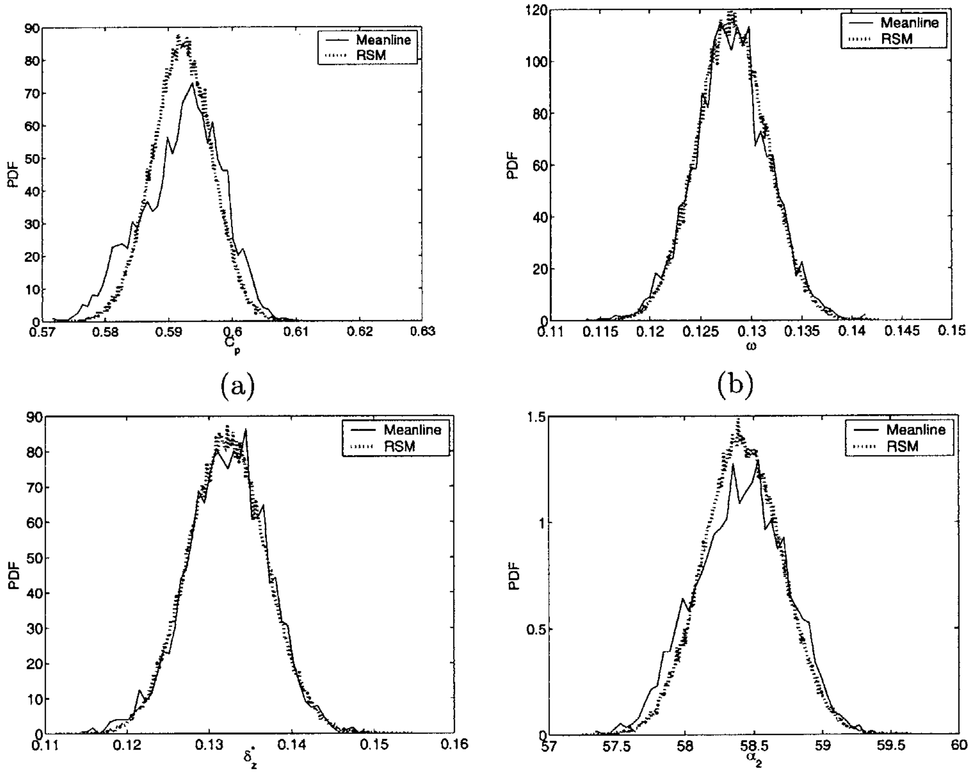

(a) (b)

(c) (d)

Figure 4-4: Response surface method (RSM) vs. model for near-stall conditions

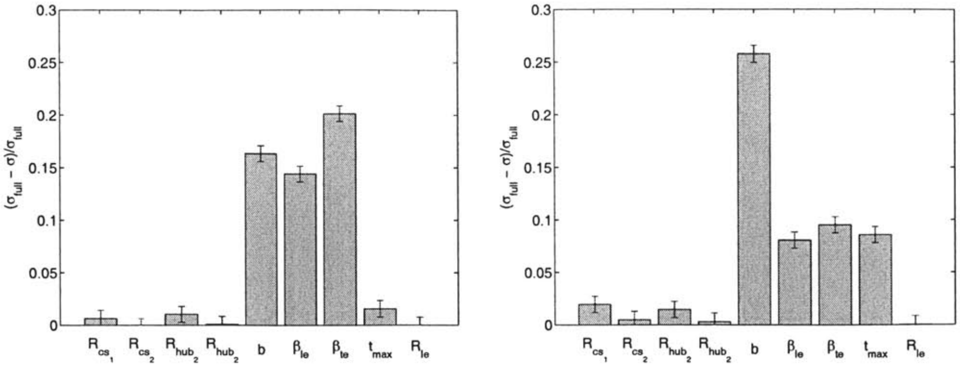

(a) Design condition

(b) Near–stall condition

Figure 4-5: C_p variability drivers

4.2.2 Parametric Analysis

The results of the parametric variability study are shown in Figures 4-5 through 4-8. The figures show the reduction in standard deviation from a Monte Carlo analysis of the RSM attained by removing the variability of the geometric parameter labeled on the abscissa. The confidence intervals for the standard deviation computed from the MCS with all variables varying, σ_{full}, and the standard deviation with one of the variables held constant, σ, are determined from Equation 3.2. The error bars in the figures show the highest and lowest values of $(\sigma_{full} - \sigma)/\sigma_{full}$ possible when both σ_{full} and σ are within their respective 95% confidence intervals.

Figure 4-5 shows that at the design condition, variability in the trailing edge angle has the greatest effect on the variability in the pressure rise coefficient; the standard deviation reduced by 20% when its variability is removed. This is due to the high stagger angle of the rotor; variations in trailing edge angle have a strong influence on the flow turning, which in turn affects pressure rise. Blade span (through tip clearance) and leading edge angle are also important contributors, with associated reductions in standard deviation of 16% and 14% respectively. Near stall, the situation changes and blade span, through the effect on tip clearance, becomes the primary driver with an associated reduction of 26%. Less important are leading edge angle, maximum thickness, and trailing edge angles with 9.5%, 8.6% and 8.1% reduction respectively.

Blade span variability drives the variation in loss coefficient at both operating conditions, as seen in Figure 4-6. At design, span accounts for 34% of the variability, followed by leading

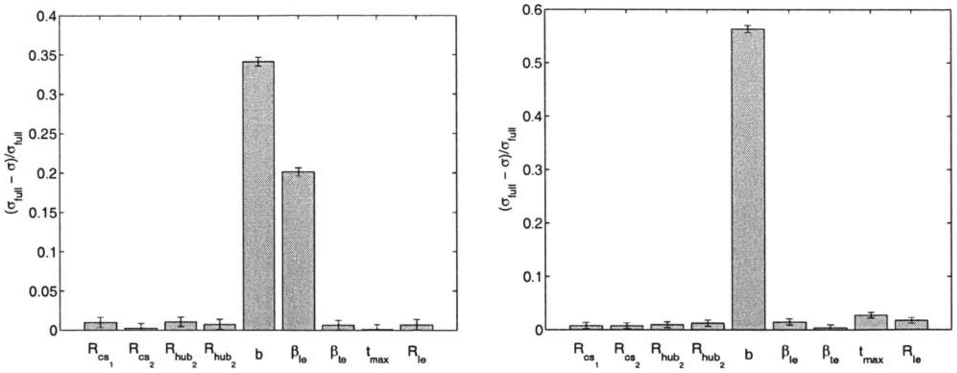

(a) Design condition (b) Near–stall condition

Figure 4-6: ω variability drivers

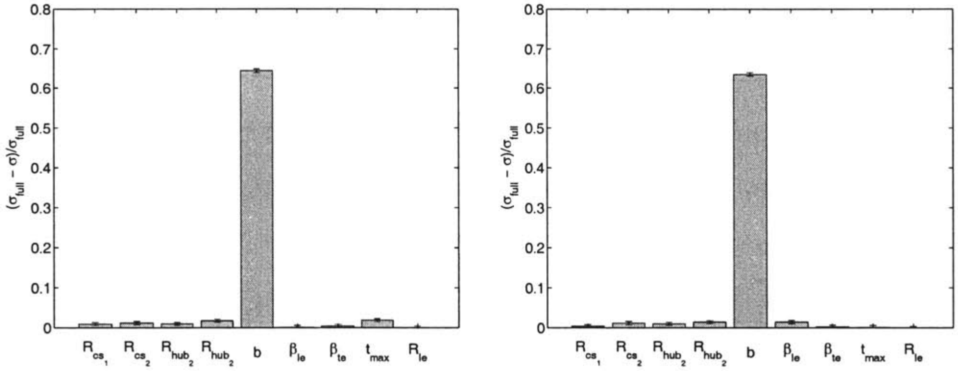

(a) Design condition (b) Near–stall condition

Figure 4-7: δ_z^* variability drivers

edge angle with 20%. Near stall, the contribution of span grows to 56%, and the individual contributions from other noise sources are small.

Blade span variability dominates displacement thickness variability, as seen in Figure 4-7. When the variability is removed, the standard deviation drops by 64% and 63% for the on-design and near-stall cases respectively. This is expected, since tip clearance variation is driven by span variation in the model, and blockage is a strong function of the clearance.

The drivers of exit angle variability are shown in Figure 4-8. At design, variability in the trailing edge angle drives the angle variation, accounting for a 28% reduction in variability. Span and leading edge angle are next important with 16% and 8%. Near stall, span is the key variability driver; its removal as a noise source reduces the angle variability by 20%. Leading edge angle, max thickness, and trailing edge angle are the next important drivers, accounting for 12%, 11%, and 8% reductions respectively.

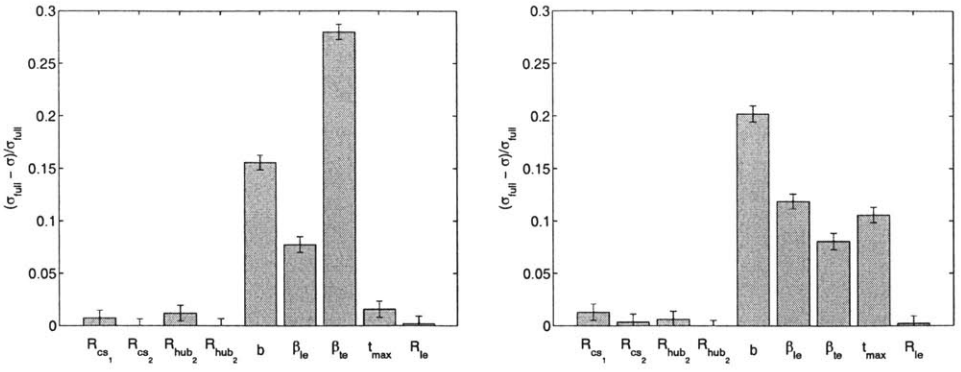

(a) Design condition (b) Near–stall condition

Figure 4-8: α_2 variability drivers

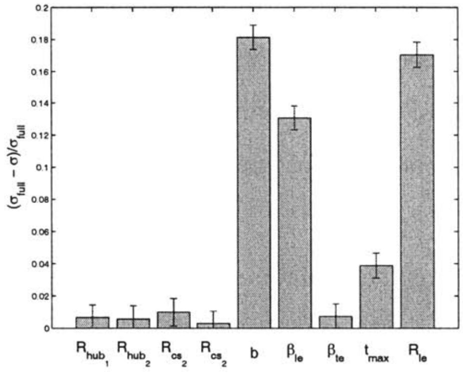

Figure 4-9: ψ_{stall} variability drivers

Blade span, through its effect on tip clearances, drives the variability in stalling pressure rise, as seen in Figure 4-9. Removal of blade span corresponds to an 18% reduction in the standard deviation of ψ_{stall}. Leading edge radius is also an important factor, accounting for a 17% reduction. Leading edge radius the third major contributor with a 13% reduction. Leading edge radius and angle affect the stalling incidence of the blade, so their importance in the variability of stalling pressure rise is not unexpected.

4.3 Sensitivity Comparison

In the previous section, blade span variability was shown to be a key driver of performance variability, presumably through its influence on tip clearance. Changes in casing and hub radii equally effect tip clearances, since $\tau = R_{cs} - R_{hub} - b$, yet the parametric analysis did not determine them to be key factors. The reason for this can be seen by examining

Table 4.5: Performance Sensitivity, $\frac{\partial(performance)}{\partial(geometry)}$

Units are [performance]/[geometry]

	on–design					near–stall			
	C_p	ω	δ_z^*/h_{nom}	α_2	ψ_{stall}	C_p	ω	δ_z^*/h_{nom}	α_2
R_{hub_1}(m)	17.9	-6.8	-9.0	14.9	5.6	22.4	-14.1	-18.3	22.7
R_{hub_2}(m)	5.7	-5.4	-9.9	2.9	5.8	13.1	-13.1	-20.3	10.3
R_{tip_1}(m)	-19.9	6.5	8.3	-15.4	-6.1	-22.2	14.1	16.6	-20.4
R_{tip_2}(m)	-2.8	5.6	10.7	-1.6	-3.8	-6.2	13.2	20.5	-5.7
b(m)	23.3	-12.3	-19.0	17.6	11.4	26.5	-27.6	-39.1	26.25
β_{le}(rad)	-0.67	0.30	0.014	-0.39	0.30	-0.42	-0.18	0.22	0.60
β_{te}(rad)	-0.79	0.046	-0.052	-0.69	-0.042	-0.47	-0.057	0.12	0.50
t_{max}(m)	-3.56	-0.091	-1.7	-2.7	2.6	-7.5	-3.4	1.2	-9.2
R_{le}(m)	-1.92	3.8	-0.71	1.6	25.7	6.1	-12.6	2.69	-4.7

the sensitivity derivatives, $\frac{\partial(performance)}{\partial(geometry)}$, calculated from fitting 40 LHS sets from the full Monte Carlo analysis of the meanline model to a first order response surface. These are shown in Table 4.5. The table indicates the performance of the rotor is as sensitive to hub and casing radii as the blade span[1], since all three parameters equally determine tip clearance.

The difference that distinguishes blade span as a variability driver in the parametric analysis is the input variability. The total variation in performance due to a given geometric parameter is a combination of the deterministic sensitivity and the probabilistic uncertainty. The although the hub and casing radii control the tip clearance equally as the span, their variability, given in Table 3.4, is smaller. Blade span variability therefore has a larger effect on tip clearance variability than hub or casing radius variability and thus a larger effect on rotor performance.

4.4 Comparison with Previous Work

Lavainne[27] conducted a deterministic sensitivity analysis of an embedded compressor stage with 3D RANS computations and used the results to construct a quadratic response surface, excluding the cross terms. A Monte Carlo analysis using SRS was run on that response surface to determine the performance variability and the key drivers. The geometric variations used were similar to those in this thesis.

Lavainne reported mean shifts in the stage efficiency and exit total pressure of $\eta - \eta_{nom} =$

---

[1] Note that the hub and casing radii at the inlet and exit of the rotor are considered separately, so the total influence is the sum of the upstream and downstream values, e.g. $R_{cs_1} + R_{cs_2}$.

-0.45% and $\frac{P_t - P_{t_{nom}}}{P_{t_{inlet}}} = -0.41\%$. The meanline model in this thesis calculated -0.4% and +0.6% mean shifts in C_p and loss coefficient near stall. The C_p mean shift at design was negligible, and the loss shift was +.4%. Loss coefficient of a blade row roughly corresponds to efficiency as $\eta \approx 1 - \omega$, so the mean shift in loss from the two approaches is similar.

The standard deviation of stage total pressure ratio and efficiency from Lavainne are reported as $\sigma_{(P_{t_{exit}}/P_{t_{inlet}})} = 0.018$ and $\sigma_\eta = 0.02$, compared to the standard deviations of static pressure and loss coefficients from this thesis of $\sigma_{C_p} = 0.0048$ and $\sigma_\omega = 0.0019$. The variability in the losses from the 3D model are an order of magnitude higher than from the present meanline model. This is mainly due to a difference in design; the rotor relative inlet Mach number in the stage from the 3D computations is close to 0.8, whereas the Mach number in this thesis is 0.15. Loss buckets become more narrow as Mach number increases and a given deviation in incidence from design will create more loss at high speed than at low speed.

The parametric analysis conducted by Lavainne showed rotor tip clearance to be the most key driver of mean shift and variability. Standard deviations of pressure ratio and efficiency were reduced by 70% and 75% respectively when tip clearance variability was removed. Trailing edge angle was the next most important for pressure ratio, and leading edge angle is important for both pressure ratio and efficiency. Near stall, tip clearance is the most important driver in this study as well as in that of Lavainne, corresponding to a 56% reduction in loss variability and a 26% reduction in pressure coefficient variability seen though variations in span. At design, leading and trailing edge angles also play important roles in pressure rise and loss variability.

In summary, although the variability attributed to the input parameters differs in the two studies, both conclude that tip clearances are the most important factor driving performance variability.

4.5 Summary

This chapter presented the results of the probabilistic analysis of a compressor rotor. A Monte Carlo analysis using 2450 Latin hypercube samples showed that pressure rise coefficient, loss coefficient, displacement thickness, and exit angle have coefficients of variations of about 1%, 3%, 4.5%, and 0.5% respectively, and the coefficients of variation are similar for on design and near stall conditions. The coefficient of variation of the stalling pressure rise was 1.1%. Mean shifts for all variables were small at both high and low flow coefficients, within 3% of the nominal.

A parametric study of the key drivers showed that blade span dominated the variability of most performance metrics at high loading. At low loading, leading and trailing edge angle variability tend to be the most significant for pressure rise and exit angle.

Chapter 5

Conclusion

5.1 Thesis Summary

A probabilistic analysis of a compressor rotor was conducted using a meanline calculation procedure that included an endwall blockage model. The procedure was broken into modules for the core and endwall flow. Blade profile loss and flow turning in the core flow were determined given the blade geometry using MISES, a quasi-3D cascade analysis software package. The core flow was coupled to the endwall though the axial displacement thickness, which controls the AVDR of the blade row. An iterative scheme was used to solve both core flow and endwall modules.

The endwall model used the analogy of a wake in a pressure gradient to calculate the development of blockage due to tip clearance leakage flow. The model extended that of Khalid et al.[23] to include the effects of double leakage. This entailed the creation of correlations for total pressure in the clearance gap and an adjustment to the leakage angle calculation. The correlations were developed using a set of 3D RANS calculations reported by Lavainne[27].

Monte Carlo simulation was used to conduct the probabilistic analysis of the meanline rotor model. The model was simulated at the design flow coefficient and a flow coefficient close to stall. At each operating condition, 49 sets of Latin hypercube samples with 50 bins each were run to conduct the probabilistic analysis. The analysis showed that the coefficient of variation remained similar for between high and low loading conditions for pressure rise coefficient, loss coefficient, displacement thickness, and exit angle. The stalling pressure rise COV was roughly 1%. Mean shifts were small for most performance parameters, typically on the order of 0.5% of the nominal.

A parametric study of the key drivers of variability was conducted using a response surface representation of the meanline model. Monte Carlo simulations of 100 LHS sets with 1000 bins were conducted with the variability of each input noise parameter individually removed. Tip clearance variation, driven by variation in blade span, was the dominant source of performance variability at the near stall condition. At the design flow coefficient, trailing edge angle was the most important source of variability for pressure rise and exit angle. Tip clearance variability was most important for loss coefficient, axial displacement thickness, and stalling pressure rise.

5.2 Recommendations for Future Work

- Construct a simple, physically based model for the evolution of blockage through a stator blade row. Such a model could be coupled with the rotor blockage model in this thesis to conduct a probabilistic analysis of a single stage or multi-stage compressor.

- It may be that an appropriate reduced description of endwall flow through multiple blade rows does not exist. In that case an alternative approach could be to conduct a series of 3D RANS calculations, building a response surface to conduct a probabilistic analysis.

- Garzon and Darmofal[15] characterized the variability in blade profile shape by conducting statistical analysis of high resolution measurements. As tip clearance has been shown to drive performance variability, a similar study (including measurements and statistical analysis) could be conducted to thoroughly quantify tip clearance variability seen in actual engines.

- Using a meanline model or a response surface of 3D calculations, an optimization study could be carried out for a given preliminary compressor design to determine the robustness of a configuration that which has been chosen to meet initial performance goals.

Appendix A

Integral Wake Calculation

This appendix details the integral wake calculation used to determine the blockage growth for the individual leakage jets in the tip clearance blockage model. The leakage jet velocity defects are modeled by 2D wakes in a pressure gradient. The details of the blockage model are hidden from the wake calculation, so the wake calculation occurs in a proverbial "black box." The calculation determines how a generic wake in a generic pressure gradient would develop given the following input parameters:

- inlet displacement thickness[1]
- inlet momentum thickness
- static pressure rise coefficient, $C_p = \frac{P_{exit} - P_{inlet}}{\frac{1}{2}\rho v_{inlet}^2}$
- streamwise distance over which the pressure changes, x_{mix}

The wake calculation outputs only the following parameters to the blockage model:

- exit displacement thickness
- exit momentum thickness
- entropy generated

The wake is calculated using a viscous-inviscid approach, coupled together by the displacement thickness. The pressure gradient in the inviscid flow far from the wake is assumed to be constant and set by the static pressure rise and x_{mix}. The velocity outside the wake, v_{∞}, is determined from this pressure gradient by Bernoulli's equation.

---

[1] For this appendix, the inlet will refer to the beginning of the pressure gradient over which the wake growth is being computed, and the exit will refer to the end of that pressure gradient.

The velocity at the edge of the wake, v_e, is described by both inviscid and viscous perspectives of the flow, diagrammed in Figure A-1. The inviscid perspective models the wake as a line source whose strength is determined by the growth in displacement thickness. The velocity far from the wake, v_{∞}, is set by the pressure rise input into the calculation. The relationship between v_{∞} and v_e is governed by potential flow theory through the wake source strength. The viscous perspective models the wake using two integral boundary layer equations, treating v_e, δ^*, and θ as unknowns. Therefore, for a given growth in displacement thickness, the viscous representation determines its own version of v_e. A coupling procedure, described in Section A.3, compares the edge velocities determined by the two perspective and a solution is is obtained when the both perspectives converge.

The rest of this appendix is dedicated to the details of the viscous and inviscid representations of the flow, as well as of the coupling procedure required to obtain a solution.

A.1 Inviscid Representation

Far from the wake, the freestream velocity profile, $v_{\infty}(x)$, is determined by the pressure gradient, which has been taken to be constant. Close to the wake, the growth in displacement thickness influences the edge velocity, v_e. As reported by Cebeci[3], the effective edge velocity can be broken up into the freestream component plus a perturbation created by the growth of the wake.

$$v_e(x) = v_{\infty}(x) + v_{pert}(x)$$

Since the wake is modeled inviscidly as a line source, the perturbation can be calculated by adding the effect of each section of the line on a given location. From boundary layer theory, the equivalent source strength of the growing wake is

$$S = \frac{\partial}{\partial x}(v_e \delta^*), \tag{A.1}$$

making the expression for the edge velocity

$$v_e(x) = v_{\infty}(x) + \int_{-\infty}^{\infty} \frac{\partial(v_e \delta^*)}{\partial x} \frac{x - x'}{(x - x')^2 + \epsilon^2} dx'; \tag{A.2}$$

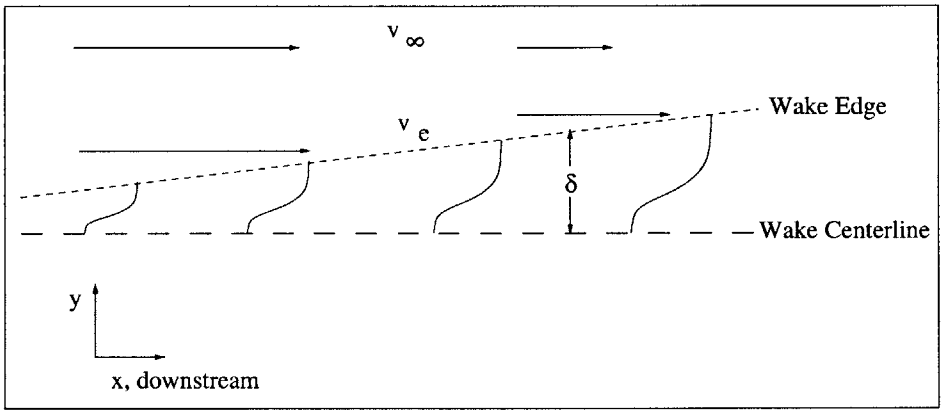
V_∞
V_e
Wake Edge
δ
Wake Centerline
y
x, downstream

(a) Viscous perspective of edge velocity

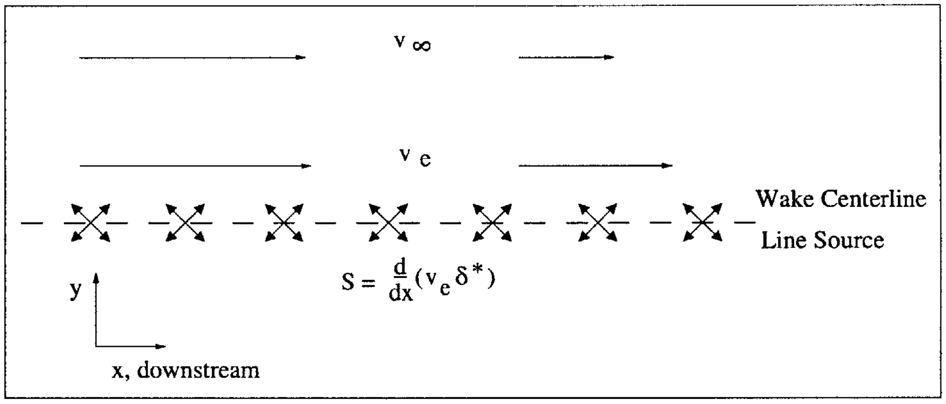
V_∞
V_e
Wake Centerline
Line Source
$S = \frac{d}{dx}(V_e \delta^*)$
y
x, downstream

(b) Inviscid perspective of edge velocity

Figure A-1: Viscous and inviscid wake representations used in Veldman[39] quasi-simultaneous coupling method where ϵ is the distance between the wake edge and the line source and is assumed to be small but non-zero.

A.2 Viscous Representation

The viscous representation of the edge velocity is defined by the momentum and kinetic energy shape parameter equations written for a wake.

$$\frac{1}{\theta}\frac{\partial \theta}{\partial x} + (H+2)\frac{1}{v_e}\frac{\partial v_e}{\partial x} = 0 \tag{A.3}$$

$$\frac{H}{H^*}\frac{\partial H^*}{\partial H}\frac{1}{\delta^*}\frac{\partial \delta^*}{\partial x} - \frac{H}{H^*}\frac{\partial H^*}{\partial H}\frac{1}{\theta}\frac{\partial \theta}{\partial x} + (1-H)\frac{1}{v_e}\frac{\partial v_e}{\partial x} = \frac{2C_d}{\theta H^*} \tag{A.4}$$

where

$$H = \frac{\delta^*}{\theta}. \tag{A.5}$$

Equation A.4 is a combination of the momentum equation and the standard kinetic energy thickness equation as described in [8].

Relations for $H^* = \theta^*/\theta$ and the dissipation coefficient C_d are derived from the wake velocity profile presented by Hill et al.[18].

$$\frac{v}{v_\infty} = 1 - \frac{\beta}{2}[1 + \cos(\frac{\pi y}{b})] \tag{A.6}$$

where β describes the extent of the velocity defect at the centerline, and b is the distance from the wake centerline to the edge. When Equation A.6 is substituted into the definitions of displacement thickness, momentum thickness, kinetic energy thickness, and dissipation, b and β can be eliminated to obtain the H^* and C_d as functions of H.

$$H^* = \frac{H^2 + 7H + 10}{9H} \tag{A.7}$$

$$C_d = K_p \frac{16\pi}{27}\frac{(H-1)^3}{H^3} \tag{A.8}$$

The dissipation coefficient C_d assumes that the turbulent eddy viscosity follows the formulation of Clauser[4], $\nu_t = K_p v_e \delta^*$ where $K_p \approx 0.016$.

With H^* and C_d defined, there is now a system of two equations (Equations A.3 and

A.4) and three unknowns (v_e, δ^*, and θ). The third equation needed to solve the system is obtained from the coupling with the inviscid flow.

A.3 Quasi-Simultaneous Coupling

There are four principal methods for solving the inviscid and viscous representations presented in Sections A.1 and A.2. Several explanations of these methods exist in the literature[10, 40], so only an overview will be presented here, framed in the context of the current calculation.

1. The direct method. An initial guess of source strength as a function of streamwise direction is specified for the inviscid representation, producing the inviscid representation the edge velocity. That edge velocity is then input into the viscous representation, which determines the displacement thickness and with it a new value of the source strength is obtained. That value is used to update the guess and the process until the source strength has converged. This method runs into difficulties for separating flows, where the viscous equations will encounter a singularity.

2. The indirect method. The opposite of the direct method, an initial guess is made for the displacement thickness and input into the viscous representation, which specifies the edge velocity. The inviscid equations then find the required displacement thickness to satisfy that edge velocity and the process is iterated. This method works well for separated flow, but has difficulties for less severe situations.

3. The semi-inverse method. Developed by LeBalleur[28], this method combines an direct inviscid representation with an indirect viscous representation. Given a guess for the source strength, both viscous and inviscid representations produce versions of the edge velocity, v_e^V and v_e^I. A new guess for the source strength is obtained by according to the difference between v_e^V and v_e^I.

4. The quasi-simultaneous method. Developed by Veldman[39], this method also combines a direct inviscid representation with an indirect viscous representation, but coupled into the viscous equations is a linear approximation to the local inviscid equations. An initial guess for the source strength is input into the inviscid equations, producing an inviscid version of the edge velocity, v_e^I, as well as a local linearization

of the inviscid flow. That local linearization is included in the system of viscous equations, and a viscous version of the edge velocity is output, v_e^V. A new guess of the source strength is then obtained from an update equation

$$S^{i+1} = S^i + \omega(\frac{\partial v_e^V}{\partial x} - \frac{\partial v_e^I}{\partial x}) \tag{A.9}$$

where ω is a relaxation coefficient, typically between 1 and 1.5. The process is iterated until $\partial v_e^V/\partial x$ and $\partial v_e^I/\partial x$ converge. This method is considered more robust than the semi-inverse method by several researchers[10, 40].

The final method, quasi-simultaneous, is the scheme used here to calculate the wakes from the individual leakage jets in the tip clearance blockage model. A local linearization of the Equation A.2 is coupled with the ordinary differential equations describing the wake. This linearization approximates how changes in source strength will affect the gradient in the edge velocity in the inviscid representation at any given streamwise location. This takes form

$$\frac{\partial v_e}{\partial x} = E_1 S + E_2. \tag{A.10}$$

where E_1 and E_2 are functions of x and can be calculated by discretizing Equation A.2 along the streamwise direction. Equation A.10 can then be coupled with Equations A.3 and A.4 to form a linear system of differential equations for the streamwise gradients of v_e, δ^*, and θ.

$$\begin{bmatrix} H+2 & 0 & 1 \\ 1-H & \frac{H}{H^*}\frac{\partial H^*}{\partial H} & -\frac{H}{H^*}\frac{\partial H^*}{\partial H} \\ \frac{1}{E_1\delta^*}-1 & -1 & 0 \end{bmatrix} \begin{bmatrix} \frac{1}{v_e}\frac{\partial v_e}{\partial x} \\ \frac{1}{\delta^*}\frac{\partial \delta^*}{\partial x} \\ \frac{1}{\theta}\frac{\partial \theta}{\partial x} \end{bmatrix} = \begin{bmatrix} 0 \\ \frac{2C_d}{\theta H^*} \\ \frac{E_0}{v_e\delta^* E_1} \end{bmatrix} \tag{A.11}$$

Given a set of initial conditions, the system in Equation A.11 can be solved numerically for using $v_e(x)$, $\delta^*(x)$, and $\theta(x)$ using a Runge-Kutta solver. The values of δ^* and θ at the exit are given as outputs to the calculation. The entropy generated is determined from the growth in kinetic energy thickness, and is output as well.

Appendix B

RSM and Meanline Model CDF Comparison

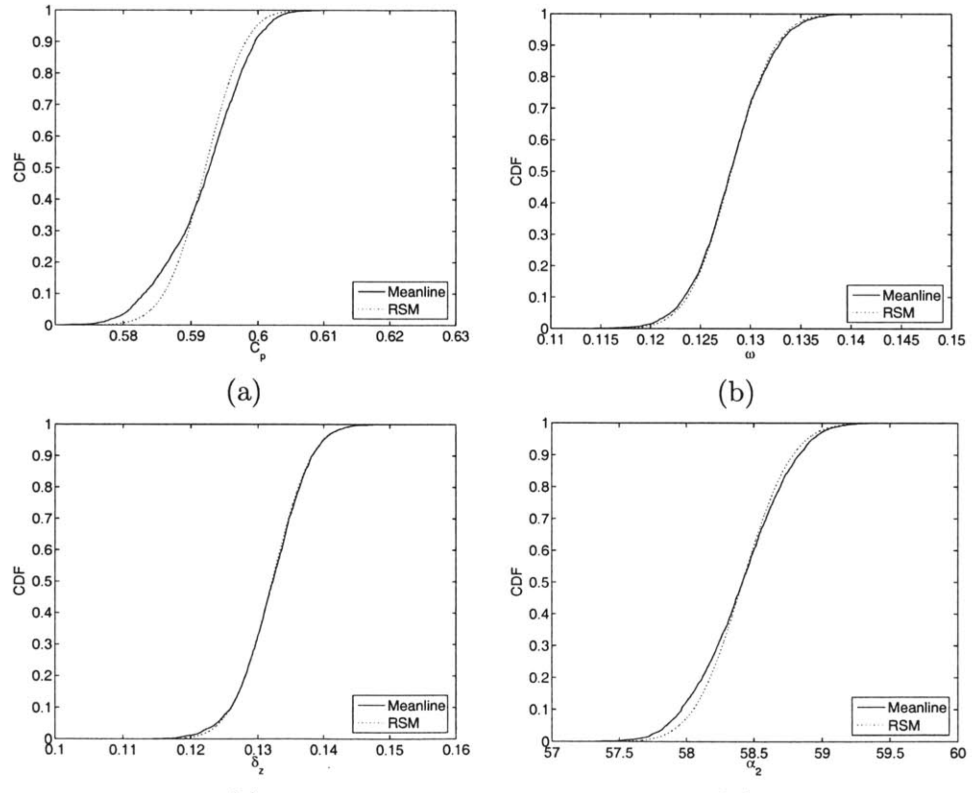

(a) (b)

(c) (d)

Figure B-1: Response surface method (RSM) vs model CDF at near-stall condition

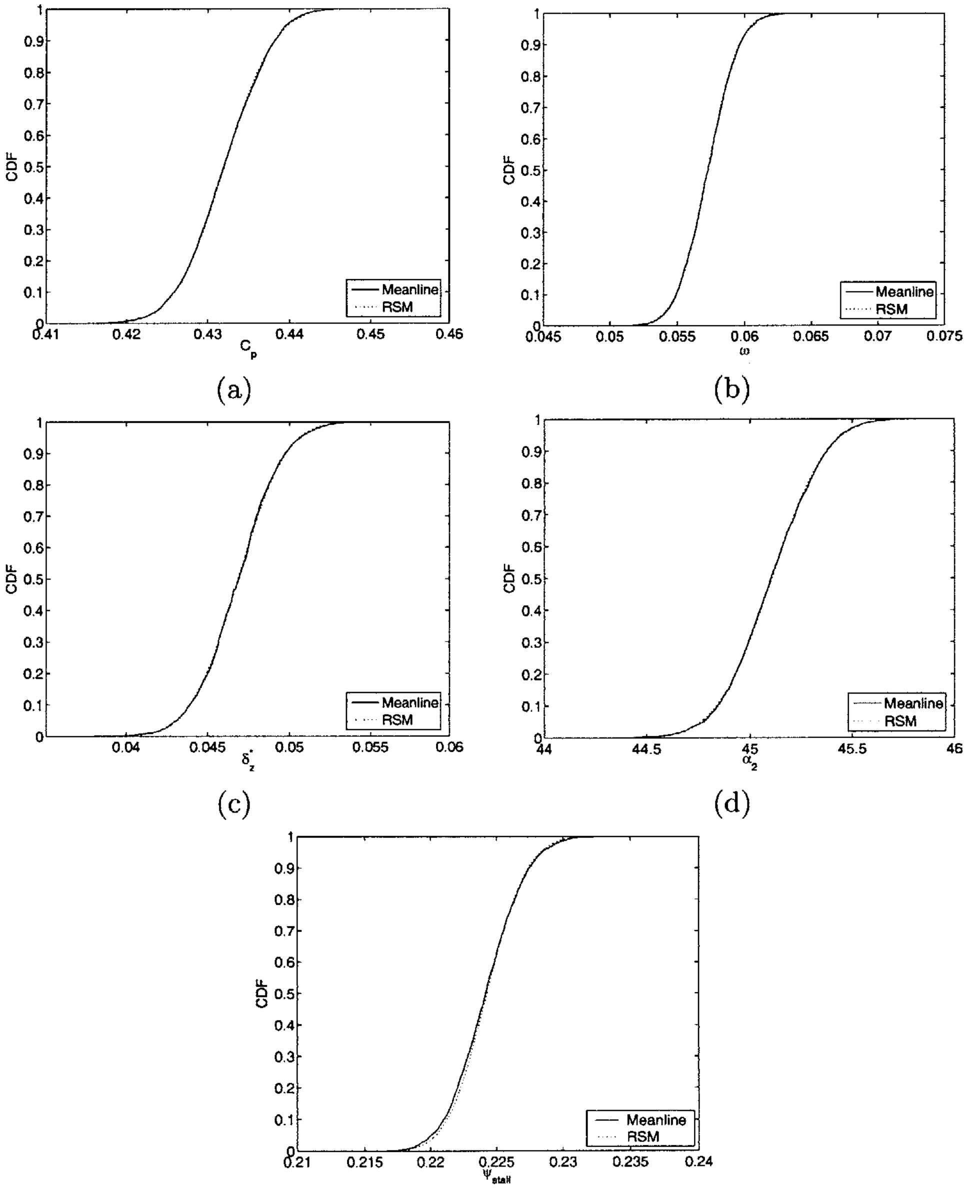

(a)

(b)

(c)

(d)

(e)

Figure B-2: Response surface method (RSM) vs model CDF at design condition

Bibliography

[1] Adkins, G. G. and Smith, L. H. "Spanwise Mixing in Axial-Flow Turbomachines." *Journal of Engineering for Power*, 104:97–110, January 1982.

[2] Ang, A. H-S. and Tang, W. H. *Probability Concepts in Engineering Planning and Design: Volume I - Basic Principles.* John Wiley & Sons, New York, 1975.

[3] Cebeci, T., Stewartson, K., and Whitelaw, J. H. "Calculation of Two-Dimensional Flow Past Airfoils." In Cebeci, Tuncer, editor, *Numerical and Physical Aspects of Aerodynamic Flows II*, pages 1–40. Springer–Verlag, 1983.

[4] Clauser, F. H. "The Turbulent Boundary Layer." In *Advances in Applied Mechanics*, volume 4, pages 1–51, New York, 1956. Academic Press.

[5] Cumpsty, N. A. *Compressor Aerodynamics.* Pearson, 1989.

[6] Dehnad, K. *Quality Control, Robust Design, and the Taguchi Method.* Wadsworth & Brooks, Pacific Grove, CA, 1988.

[7] Dong, Y. Personal Communication, 2004.

[8] Drela, M. and Giles, M. B. "Viscous-Invisid Analysis of Transonic and Low Reynolds Number Airfoils." *AIAA Joural*, 25(10):1347–1355, October 1987.

[9] Drela, M. and Youngren, H. *A User's Guide to MISES 2.53.* MIT Fluid Dynamics Research Laboratory, 70 Vassar St, Cambridge MA 02139, December 1998.

[10] Edwards, D. E. and Carter, J. E. "A Quasi-Simultaneous Finite Difference Approach for Strongly Interacting Flow." In Cebeci, Tuncer, editor, *Numerical and Physical Aspects of Aerodynamic Flows III*, pages 126–142. Springer–Verlag, 1985.

[11] Fishman, G. S. *Monte Carlo: Concepts, Algorithms and Applications.* Springer Verlag, New York, 1996.

[12] Gallimore, S. J. "Spanwise Mixing in Multistage Axial Flow Compressors: Part II - Throughflow Calculations Including Mixing." *ASME Journal of Turbomachinary*, 108:10–16, 1986.

[13] Gallimore, S. J. and Cumpsty, N. A. "Spanwise Mixing in Multistage Axial Flow Compressors: Part I - Experimental Investigation." *ASME Journal of Turbomachinary*, 108:2–9, 1986.

[14] Garzon, V. E. *Probabilistic Aerothermal Design of Compressor Airfoils.* PhD thesis, Massachusetts Institute of Technology, 2003.

[15] Garzon, V. E. and Darmofal, D. L. "Impact of Geometric Variablility on Axial Compressor Performance." *Journal of Turbomachinary*, 125(4):692–703, October 2003.

[16] Gong, Y., Tan, C. S., Gordon, K. A., and Greitzer, E. M. "A Computational Model for Short Wavelenght Stall Inception and Development in Multi-Stage Compressors." *Journal of Turbomachinary*, 121(4):726–734, 1999.

[17] Greitzer, E. M. and Wisler, D. C. "Gas Turbine Compressor Technology: Status and Opportunities." Keynote Lecture at International Gas Turbine Congress, Kobe, Japan, 1999.

[18] Hill, P. G., Schaub, U. W., and Senoo, Y. "Turbulent Wakes in Pressure Gradients." *Journal of Applied Mechanics*, pages 518–524, December 1963.

[19] Horlock, J. H. "The Determination of End-Wall Blockage in Axial Compressors: A Comparison Between Various Approaches." *Journal of Propulsion and Power*, 16:57–64, January 2000.

[20] Horlock, J. H. and Perkins, H. J. "Annulus Wall Boundary Layers in Turbomachines." AGARDograph 185, 1974.

[21] Hunter, I. H. and Cumpsty, N. A. "Casing Wall Boundary-Layer Development Through an Isolated Compressor Rotor." *Journal of Engineering for Power*, 104:805–817, October 1982.

[22] Khalid, S. A. *The Effects of Tip Clearance on Axial Compressor Pressure Rise.* PhD thesis, Massachusetts Institute of Technology, 1995.

[23] Khalid, S. A., Khalsa, A. S., Waitz, I. A., Tan, C. S., Greitzer, E. M., Cumpsty, N. A., Adamczyk, J. J., and Marble, F. E. "Endwall Blockage in Axial Compressors." *Journal of Turbomachinary*, 121(3):499–509, July 1999.

[24] Khalsa, A. S. *Endwall Blockage Blockage in Axial Compressors.* PhD thesis, Massachusetts Institute of Technology, 1996.

[25] Koch, C. C. "Stalling Pressure Rise Capability of Axial Flow Compressor Stages." *Journal of Engineering for Power*, 103:645–656, October 1981.

[26] Koch, C. C. and Smith, L. H. "Loss Sources and Magnitudes in Axial-Flow Compressors." *Journal of Engineering for Power*, pages 411–425, July 1976.

[27] Lavainne, J. "Sensitivity of a Compressor Repeating-Stage to Geometry Variation." Master's thesis, Massachusetts Institute of Technology, September 2003.

[28] LeBalleur, J. C. "Couplage Visqueux-Non Visqueux: Methode Numerique Et Applications Aux Ecoulements Bidimensionnels Transsoniques Et Suersoniques (Viscous-Inviscid Flow Matching: Numerical Method and Applications to Two-Dimensional, Transonic and Aupersonic Flows)." *La Recherche Aerospatiale*, pages 65–76, March 1978. ESA-TT-496.

[29] Lykins, C., Thompson, D., and Pomfret, C. "The Air Force's Application of Probablilistics to Gas Turbine Engines." AIAA 94-1440-CP, 1994.

[30] Manteufel, R. D. "Evaluating the Convergence of Latin Hypercube Sampling." AIAA 2000-1636, 2000.

[31] Martinez-Sanchez, M. and Gauthier, R. P. "Blade Scale Effects of Tip Leakage." Gas Turbine Laboratory Report 202, Massachusetts Institute of Technology, Cambridge, Massachusetts, 1990.

[32] Mavris, D. N. "A Methodology for Robust Design of Impingement Cooled HSCT Combustor Liners." AIAA 97-0288, 1997.

[33] Mellor, G. L. and Wood, G. M. "An Axial Compressor End-Wall Boundary Layer Theory." *Journal of Basic Engineering*, pages 300–316, July 1971.

[34] Owen, A. B. "A Central Limit Theorem for Latin Hypercube Sampling." *Journal of the Royal Statistical Society. Series B*, 54(2):541–551, 1992.

[35] Smith, L. H. "Casing Boundary Layers in Multistage Axial-Flow Compressors." In Dzung, Lang S., editor, *Flow Research on Blading*, pages 275–304, Amsterdam, Netherlands, 1970. Elsevier Publishing.

[36] Stein, M. "Large Sample Properties of Simulations Using Latin Hypercube Sampling." *Technometrics*, 29(2):143–151, 1987.

[37] Storer, J. A. *Tip Clearance Flow in Axial Compressors.* PhD thesis, Cambridge University, 1991.

[38] Storer, J. A. and Cumpsty, N. A. "An Approximate Analysis and Predition Method for Tip Clearance Loss in Axial Compressors." *Journal of Turbomachinery*, 116:648–656, 1994.

[39] Veldman, A. E. "New, Quasi-simultaneous Method to Calculated Interacting Boundary Layers." *AIAA Journal*, pages 79–85, 1981.

[40] Williams, B. R. and Smith, P. D. "Coupling Procedures for Viscous-Inviscid Interaction for Attached and Separated Flow on Swept and Tapered Wings." In Cebeci, Tuncer, editor, *Numerical and Physical Aspects of Aerodynamic Flows IV*, pages 53–70. Springer–Verlag, 1983.

[41] Wisler, D. C. "Core Compressor Exit Stage Study, Volume I - Blading Design." NASA CR-135691, 1977.

[42] Wisler, D. C., Bauer, R. C., and Okiishi, T. H. "Secondary Flow, Turbulent Diffusion, and Mixing in Axial-Flow Compressors." *Journal of Turbomachinery*, 109:455–482, October 1987.